

Estimating forces during ploughing of a granular bed

Prasad Sonar^{1,†}, Sachin Modi¹ and Ishan Sharma¹

¹Mechanics and Applied Mathematics Group, Department of Mechanical Engineering, Indian Institute of Technology Kanpur, UP 208016, India

(Received 18 March 2018; revised 18 June 2019; accepted 18 June 2019;
first published online 19 July 2019)

We present a method for predicting forces on a plough – modelled as a flat, rigid plate inclined in the direction of motion – as it moves through a granular bed. Our method combines coarse, but representative, discrete element (DE) simulations with continuum mechanics. We first homogenize the kinematic information obtained from DE simulations to obtain a continuum strain field. The strain field is then combined with an appropriate continuum constitutive law for the granular material being ploughed and linear momentum balance to obtain forces acting on the plough. Our method has the advantage that it does not require (i) detailed DE simulations nor (ii) extensive calibration of grain parameters to match experiments which, in turn, requires significant effort and may be system dependent. Both (i) and (ii) are necessary if forces are to be estimated directly from simulations. We confirm the effectiveness of our approach by comparing our predictions with results from calibrated DE simulations and experiments.

Key words: granular media

1. Introduction

Ploughing or excavation (figure 1) is an important process that finds application in industries like agriculture, mining, construction and earth-moving. Modelling such processes is challenging because of the complex nonlinear behaviour of granular material, its spatial variability and the dynamic effects that may occur during rapid granular flow. Ploughing is a power-intensive process and the prediction of forces on the plough is essential for better machine design. At the same time, estimating forces on fully or partially submerged objects moving relative to a granular medium remains a problem of fundamental importance; see, e.g. Wieghardt (1975), Bharadwaj, Wassgren & Zenit (2006), Seguin *et al.* (2011) and Katsuragi & Durian (2013).

Various methods have been developed in the past to study the ploughing process. Analytical methods are based on Terzaghi's passive soil pressure theory (Hettiaratchi, Witney & Reece 1966; McKyes & Ali 1977). These methods model the failure pattern in granular media and take the process to be quasi-static. Sokolovski (1960) employed slip-line theory, which assumes that failure inside the bulk occurs at certain planes. In these methods complicated plough geometries and dynamic effects cannot be taken

† Email address for correspondence: prasads@iitk.ac.in

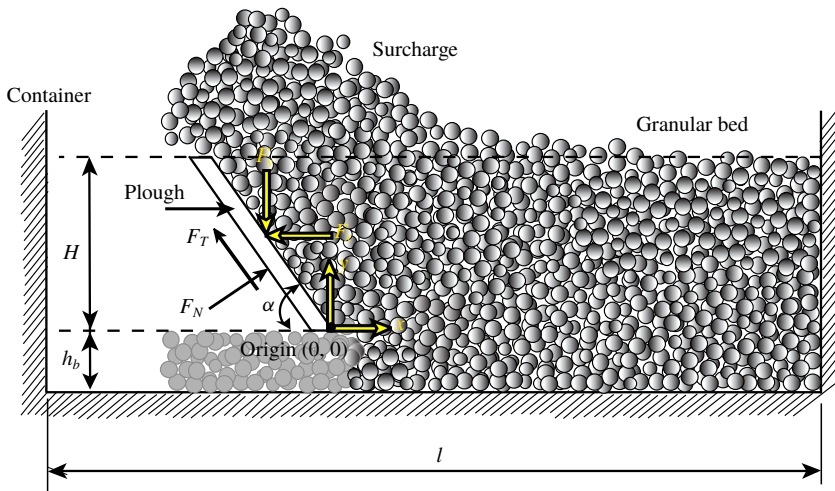


FIGURE 1. (Colour online) Schematic of ploughing, where a flat, rigid, inclined plough moves through a granular bed. The coordinate system $(x-y)$ in which we will work is attached to the plough's tip. The inclination angle of the plough is α , H is the depth of the plough in the granular bed measured from the undisturbed bed's surface, h_b is the distance of the plough's tip from the base of the container and l is the length of the container. The plough moves to the right at speed v_c . The force acting on the plough may be split along and normal to the plough as, respectively, F_N and F_T , or along the given $(x-y)$ coordinate system as F_x and F_y , respectively. In the main text we will typically compute F_x and F_y .

into account. Furthermore, slip-line theory is limited to two dimensions and to rigid perfectly plastic materials. At the same time, analytical methods developed for three dimensions (Hettiaratchi & Reece 1967) make many simplifying assumptions and are restricted to quasi-static processes. Recently Gravish, Umbanhowar & Goldman (2010) fitted their experimental results about forces in ploughed grains through the method of wedges (Nedderman 1992), which is a quasi-static technique. Finally, we mention the work of Palmer (1999) and Sauret *et al.* (2014). Sauret *et al.* (2014) investigated bulldozing of granular material through experiments and continuum depth-averaging techniques, but did not compute the forces exerted by the granular flow on the plough. Palmer (1999) explored the effect of speed during rapid cutting of water-saturated soils. An analytical model is developed for the change in pore pressure, and the increase in cutting effort is explained through a drop in pore pressure which augments effective stresses. Models/techniques to predict the cutting forces are not developed. In contrast, our work concerns dry granular materials, and we put forward a methodology to estimate forces during cutting (ploughing).

Ploughing involves large deformations during which grains may lose or come into contact. Because of this, it becomes difficult to model ploughing of a granular bed through finite element methods. Most current studies employ the discrete element (DE) method, developed by Cundall & Strack (1979), or its extensions. Examples of application of the DE method to processes like ploughing and soil cutting include Ono *et al.* (2013), who studied soil cutting resistance using three-dimensional DE simulations, Asaf, Rubinstein & Shmulevich (2007), who analysed cutting blade shapes using two-dimensional DE simulations, and Coetzee (2014), who compared

the efficacy of DE and continuum (material point) methods in modelling soil cutting. The experiments of Percier *et al.* (2011) and Guo *et al.* (2012) on forces experienced during ploughing were also explained using two-dimensional DE simulations. Guo *et al.* (2012), additionally, employed an extended Coulomb's Earth pressure theory (Nedderman 1992) to model their observations. This was consistent because Guo *et al.* (2012) ploughed at very slow rates.

Gravish, Umbanhowar & Goldman (2014) recently utilized resistive force theory (RFT) to estimate forces during ploughing. This technique was initially developed for computing the drag on intruders in viscous fluids, and then later extended to intruders in granular media (Li *et al.* 2009; Ding, Gravish & Goldman 2011). In RFT, the total load on an intruder is found by dividing the intruder into smaller elements, computing the loads on these elements separately either through experiments or simulations, and then assuming that the total load on the intruder is the sum of the loads on all its elements. Thus, a fundamental assumption is that the loads experienced by an element of the intruder are unaffected by the presence of the rest of the intruder (Aguilar *et al.* 2016; Askari & Kamrin 2016; Slonaker *et al.* 2017). Even in isolation, the force per unit area acting on each intruder element depends upon its orientation and velocity, and the flow velocity of the grains. At the same time, as part of the intruder, the orientation and velocity of an element, and the flow's local velocity will vary, and may even change. Thus, the force on an isolated intruder element for a range of velocities and orientations has to be found, and then superposed to find the total load on the intruder. A complete physical and mathematical explanation of why superposition of forces employed in RFT succeeds in nonlinear systems like granular flows is unavailable, although Askari & Kamrin (2016) have attempted to provide necessary conditions to predict the materials wherein RFT may work. We list the main differences between RFT and our approach in § 2.

A central challenge in applying the DE method directly to granular flows is the calibration of the grain micro-properties. This is necessary to ensure that the virtual (i.e. simulated) granular material displays the macroscopic constitutive response of the grains being investigated. Parameters entering the interaction law governing grain-to-grain contact in the DE simulations are determined using theory, trial-and-error or experiments. Coetzee (2017) reviews the many calibration procedures employed by various researchers. For example, Tanaka *et al.* (2000) compared the results of DE simulations with actual bar penetration tests. They varied the friction coefficient between grains to determine the value that provided the best comparison. Shmulevich, Asaf & Rubinstein (2007) found interaction parameters from *in situ* field tests. They compared their test results and simulations and applied a nonlinear optimization algorithm to locate optimal grain parameters for use in simulations. Coetzee & Els (2009) employed a combination of shear tests and compressions tests of grains simulated through the DE method, and compared these results with experimentally measured friction angle and stiffness to determine the best set of grain friction and grain stiffness values. Thus, calibration (i) requires significant effort, (ii) is often application specific and (iii) is not standardized.

Even after the grain parameters have been calibrated for an application, in order to obtain accurate and robust force data with low noise, it is found necessary to employ a very large number of grains. For example, Tsuji *et al.* (2012) employed 300 000 grains in their simulation of bulldozing. Sometimes even grain shapes have to be modelled more exactly than as mere spheres; for example, Coetzee & Els (2009) employed clumped spherical grains to model the shape of corn grains used in their experiments. These aspects significantly increase the computational cost.

Here, we propose to obtain forces during ploughing by combining kinematic data obtained from coarse, but representative, DE simulations with continuum mechanics. This approach circumvents the necessity of extensive calibration of DE simulations, and also does not require a very large number or complex shapes of grains. Computational cost is, thus, significantly lowered and, at the same time, greater insight is obtained into which kinematic aspects of the flow affect its kinetics the most. We identify our approach as the extended strain path method (ESPM), as its spirit is somewhat similar to the strain path method developed by Baligh (1985) for deep, quasi-static penetration processes. The main differences (and advantages) being that ESPM is applicable to dynamic processes, and may be applied to those granular flows in which strain paths are not easily visualized in experiments. We develop and demonstrate ESPM in the context of two-dimensional ploughing. Additionally, we employ a simple rheology for the granular flow, in order to keep the number of fitted parameters to a minimum. The method may, however, be extended to three dimensions and more complex rheologies.

Computing the continuum velocity field of the flowing grains is a fundamental step in ESPM. Deformation fields for applications similar to ours have been studied in the past using various techniques, and we briefly summarize them. Wettergreen *et al.* (2010) and Loret de Mola Lemus *et al.* (2014) investigated the motion of a rover on sand and controlled it by actuating a plough. The force on the plough required for braking is measured in terms of wheel slip. Moreland *et al.* (2012) visualized the complex soil flow patterns under a wheel using a shear interface imaging analysis tool. The deformation fields obtained were for soil–wheel interaction, and are not directly relevant to our case.

Murthy, Gnanamanickam & Chandrasekar (2012) and Yadav, Saldana & Murthy (2015) obtained deformation fields during indentation of a granular bed in a rectangular chamber. It is important to note that, because metals can withstand significant tensile forces while, in contrast, granular materials have almost no tensile strength, many of the features observed in metals, especially at the surface, may not be found in grains. Finally, Murthy *et al.* (2013) performed soil cutting experiments with a vertical plough, and generated velocity contour maps using image analysis; these, as we will see in §4.1, resemble what we find in simulations.

In passing we mention some recent techniques that have been employed to measure the large deformation inherent in granular materials. These include fine grid techniques (Sevenhuijsen, Sirkis & Bremond 1993; Goldrein, Palmer & Huntley 1995), which analyse images of distorted surface grids to produce quantitative displacement and strain maps, and digital speckle X-ray flash photography (Goldrein *et al.* 2002; Grantham *et al.* 2006), which combines digital speckle photography with flash X-ray photography to measure two- and three-dimensional displacement fields within bodies undergoing dynamical deformation.

Finally, we mention the work of Qiong, Pitt & Ruina (1986) who found forces exerted by soil on a plough mouldboard by constructing strain paths from scratch traces left on the mouldboard. In this, they too followed a strain path method. However, assumptions about the flow that they made, while perfectly suitable for a mouldboard, are not easily extended to other flows, such as the one investigated here.

The rest of the paper is organized as follows. We discuss ESPM in the next section. Our DE simulations, from which we obtain kinematic data, are described in §3. We then obtain the continuum strain rate field in §4 by homogenizing the position data computed from DE simulations. Next, we test the extent of the applicability of ESPM by probing the degree to which ploughing is kinematically controlled. We then

introduce a continuum model of the granular flow in §5 and combine it with the strain rates obtained from DE simulations and linear momentum balance to calculate stresses in the bulk. This, subsequently, allows us to estimate forces on the plough. Finally, in §6 we present our results. We observe a good match between our ESPM predictions and calibrated DE simulations, and also with experiments conducted by us and others.

2. Extended strain path method

The ESPM combines DE simulations and continuum analysis and has the following main steps.

- Step 1:* Obtain an approximation to the strain rate field, while modelling the granular material as a continuum. This may be done through experiments, e.g. Baligh (1985) or Qiong *et al.* (1986), or simulations, as we propose. Here, we employ representative DE simulations that are fairly coarse and do not employ calibrated grain properties. Hence, the total computational effort is much lower than purely computational paradigms (e.g. Coetzee 2014).
- Step 2:* Select an appropriate continuum constitutive description of the flowing grains. We will model the granular material as a pressure-dependent Bingham fluid (Sharma 2017, § 2.10.1), which is very similar to the $\mu(I)$ -rheology proposed by Jop, Forterre & Pouliquen (2006). A Bingham fluid (Oldroyd 1947; Prager 1961, p. 136) has the property that it remains rigid until the stresses violate a yield criterion, after which it flows. The yield criterion may or may not be pressure-dependent, and we employ a pressure-dependent yield criterion to match with observed behaviour in granular materials. We employ a simple rheology in order to minimize the number of fitted parameters.
- Step 3:* Combine the strain field of step 1 with the constitutive description of step 2 and linear momentum balance to obtain the stress field in the granular material being ploughed. From this the forces acting on the plough may be estimated.

Implicit in this approach is the assumption that deformations during ploughing are greatly constrained by the system's geometry, to the extent that the strain rate field does not vary significantly for media containing grains with different properties, e.g. size, shape, texture, density, inelasticity. Thus, the strain rate field may be estimated fairly accurately without matching the actual properties of the grains in the material being ploughed. We will test the validity of this assumption by performing DE simulations with several different choices of grain parameters: friction coefficients, grain sizes and polydispersities. At the same time, we emphasize that our ultimate aim is to predict the forces on the plough and not the strain field. Thus, variations in the strain rates that appear significant from a kinematic viewpoint may, in fact, not be that consequential to the kinetics.

Our approach above is somewhat similar to the strain path method developed by Baligh (1985) for geotechnical problems, specifically deep penetration problems. Similar kinematic-based analyses that utilize hydrodynamic models have been developed for modelling high-velocity impacts into metals (see, e.g. Birkhoff *et al.* 1948; Alekseevskii 1966; Tate 1967, 1969, 1978, 1986*a,b*; Yarin, Rubin & Roisman 1995; Rubin 2012; Sharma 2019). Baligh (1985) guessed or estimated the strain field from penetration experiments in saturated clays. In contrast, the strain field

for ploughed grains has not been reported. In our approach, we obtain kinematic information from representative, but coarse and uncalibrated, DE simulations. We therefore identify our approach as an ESPM. The advantage is that, with DE simulations, we are able to visualize the kinematics of granular flows in complex and/or three-dimensional geometries that may be inaccessible to experiments. Furthermore, ESPM may be utilized in dynamic processes where inertia plays a role. These features will allow application of ESPM to many more processes.

Finally, we list the main differences between RFT (Gravish *et al.* 2014) and ESPM:

- (i) RFT estimates forces on intruders in granular flows, while ESPM may also be employed for flows across infinite surfaces.
- (ii) RFT does not describe the flow and stress fields in the granular media, while ESPM can estimate them.
- (iii) ESPM finds the flow kinematics from coarse DE simulations without a great need for matching grain parameters in the DE simulations (cf. §4.3). Thus, one DE simulation provides all kinematic information necessary for flows of different types of grains, but the same system geometry. The constitutive law accounts for the difference in grain types. In contrast, RFT requires multiple experiments/simulations to map out forces at all orientations and velocities of an intruder element, which will have to be repeated when the grain type is changed. Li, Zhang & Goldman (2013) suggest that information for different orientations and grain types could be obtained by scaling/fitting laws for flat-faced planar elements. However, the accuracy and efficacy of these fits have not yet been documented comprehensively.
- (iv) In ESPM, the effort required to simulate flows over complex geometries (e.g. curved ploughs) is comparable to that of simpler shapes like flat-faced ploughs. In contrast, RFT may entail a larger number of experiments/simulations. It is also possible that planar elements may not work for more complicated shapes. To that extent, ESPM may be easier to implement for complex geometries.
- (v) Finally, it is unclear how RFT will work in transient problems. In contrast, ESPM can be extended to transient problems by utilizing transient DE simulations.

We will now apply ESPM to find the forces required during ploughing of a granular bed in two dimensions. We will begin by describing our DE simulations that are required in step 1 above.

3. Simulation methodology

3.1. Geometry

Figure 1 shows a schematic of a typical two-dimensional ploughing operation with a flat, rigid, inclined plough. To set up our DE simulations, first a bed of grains is prepared by dropping grains in a rectangular container freely under gravity. The container has a length of 200 non-dimensional units. Table 1 lists relevant non-dimensional parameters. To prevent lattice formation, equal amounts of two differently sized grains with diameters in the ratio of 1:0.7 were taken. This ensures a spatially random distribution of grains. Bhateja, Sharma & Singh (2016, 2017) provides details of our DE simulations. The plough is also made up of disc-shaped grains with half the diameter of the larger grains; see inset in figure 3. This method of modelling the plough allows us to readily model any shape of plough.

Once the bed is prepared, the plough moves from the left to the right at a constant velocity. We note from figure 1 that the rectangular container has a wall at its right

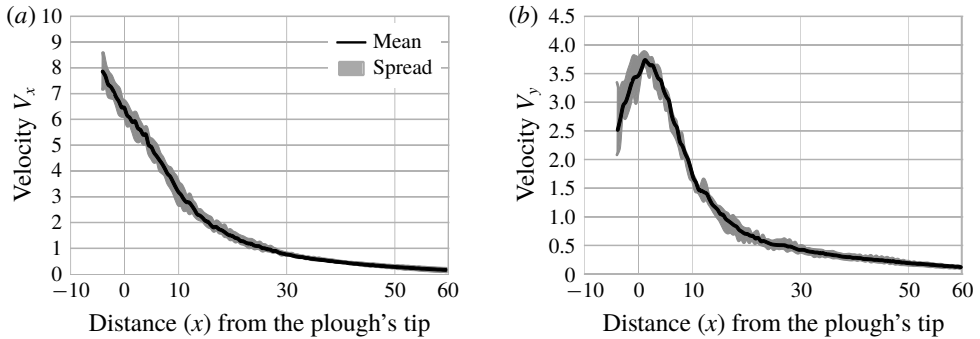


FIGURE 2. The continuum velocity field associated with the granular material, calculated as per § 4.1, is plotted at points along the line $y=9$. The velocity field was computed at five time instants during the time in which the plough's tip moves from $x=50$ to 130, which corresponds to a distance of 150 to 70 non-dimensional units away from the right-hand boundary. The mean of these five samples (black curve) and the spread about the mean (grey region) are shown. (a) Velocity V_x along x . (b) Velocity V_y along y . The plough's non-dimensional speed $v_c=10$, the inter-grain friction $\mu=0.3$ and grain diameter $d=0.67$.

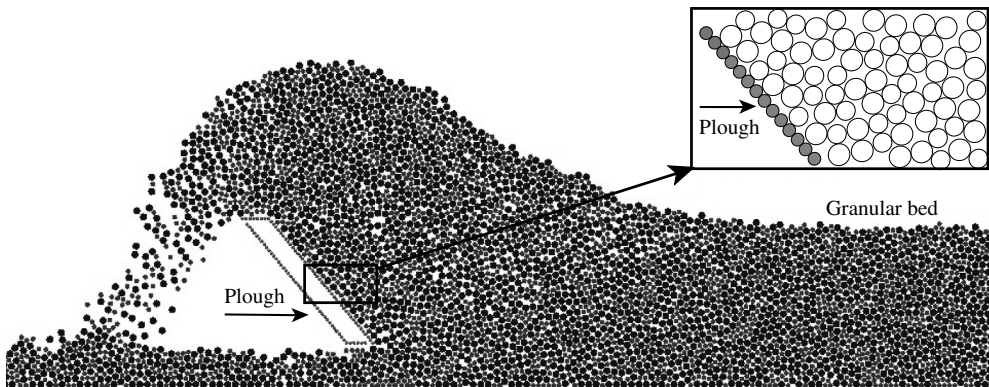


FIGURE 3. Snapshot from a DE simulation. The inset shows details of how the plough is modelled. We modelled the plough by arranging plough-grains in a straight line close to each other. The size of these grains compared to that of flowing grains defines the smoothness of the plough's surface. Rearranging the grains to follow a defined trajectory would allow us to readily model any shape of plough.

end. This is required to define the computational domain. This wall does not affect the flow until it is less than 70 non-dimensional units away from the plough's tip. As shown in figure 2, the flow of grains is steady when the plough travels between 50 and 130 non-dimensional units from the left-hand side wall (see caption). Figure 3 shows a snapshot from the DE simulation of the flow at steady state.

Finally, we note that in simulations it is possible to both allow or restrict rotation of the grains. We compare outcomes from the two in § 4.3.1 and show that both choices provide essentially the same strain rate fields. Subsequently, we only utilize simulations wherein grain rotations are restricted.

Dimensionless parameter	Scaling factor	Scaled value
Length of granular bed, l	l	200
Depth of cut, H	l	10
Grain diameters, d_1 and d_2	l	0.67 and 0.47
Grain friction coefficient, μ	–	0–1
Ploughing velocity, v_c	\sqrt{gl}	0.1–20
Angular velocity, ω_c	l/\sqrt{gl}	–
Inclination angle, α	–	50°
Spring constant, k_n and k_t	mg/l	10 ⁶
Mass of larger grain, m	m	0.45
Restitution coefficient, e_n	–	0.5
Time step, Δt	$\sqrt{l/g}$	10 ^{–4}
Acceleration, a	g	–
Force, f	mg	–

TABLE 1. Dimensionless parameters employed in simulations.

4. Kinematics

All computations are done in a coordinate system attached to the plough’s tip, as shown in figure 1. Unit vectors \hat{i} and \hat{j} point along x and y directions, respectively.

4.1. Continuum velocity field

Our ESPM requires the continuum velocity field V to obtain strain rates. From DE simulations we obtain position data for each grain at every time step. Velocities of grains are calculated by noting displacements at short time intervals and dividing them by the time interval. The time interval is chosen small enough so as to restrict displacement to less than one grain diameter. The position of a grain is taken to be the mean of the positions at the beginning and at the end of the time interval. Thus, if \mathbf{r}_p^n and \mathbf{r}_p^{n+1} are the positions of the p th grain at times t^n and t^{n+1} , respectively, then we define the grain velocity

$$\mathbf{U}(\mathbf{r}_{n+1/2}, t_{n+1/2}) = \frac{\mathbf{r}_p^{n+1} - \mathbf{r}_p^n}{t^{n+1} - t^n}, \quad \text{where } \{\mathbf{r}_{n+1/2}, t_{n+1/2}\} = \left\{ \frac{\mathbf{r}_p^n + \mathbf{r}_p^{n+1}}{2}, \frac{t^n + t^{n+1}}{2} \right\}. \quad (4.1)$$

Thus, the velocity of each grain is obtained as a function of position at different time steps. The flowing grains are now thought to constitute a continuum. We next extract a continuum velocity field from $\mathbf{U}(\mathbf{r}_{n+1/2}, t_{n+1/2})$.

A fixed square grid with a grid size of 0.5 non-dimensional units is constructed covering the region of interest; see figure 4. The continuum’s velocity field $\mathbf{V}(x, y, t)$ at any time t is obtained at a point (x, y) of this grid by averaging the velocities \mathbf{U} of the grains whose centres lie within the square grid, as demonstrated in figure 4. Once the velocity field is known, the acceleration may be calculated through

$$\mathbf{a} = \frac{\partial \mathbf{V}}{\partial t} + \nabla \mathbf{V} \cdot \mathbf{V}. \quad (4.2)$$

The continuum velocity field \mathbf{V} thus obtained at different time instants is noisy due to inherent fluctuations of the flowing grains. In a steady flow, we average the

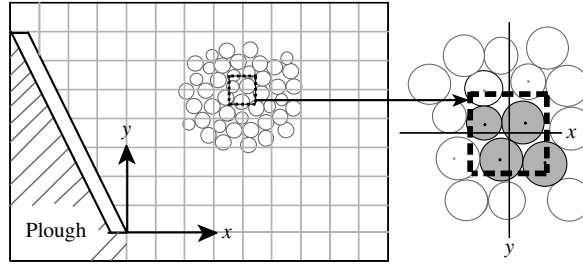


FIGURE 4. Schematic of the square grid employed to post-process data obtained from DE simulations. The inset shows a square (dashed lines) of size 0.5×0.5 constructed around the grid point (x, y) . The velocities of all shaded grains, whose centres lie within the square, are averaged, and the resultant velocity is assigned to the grid point (x, y) . Grains lying in hatched region are not relevant to our computations and are, therefore, ignored. Figure is not to scale.

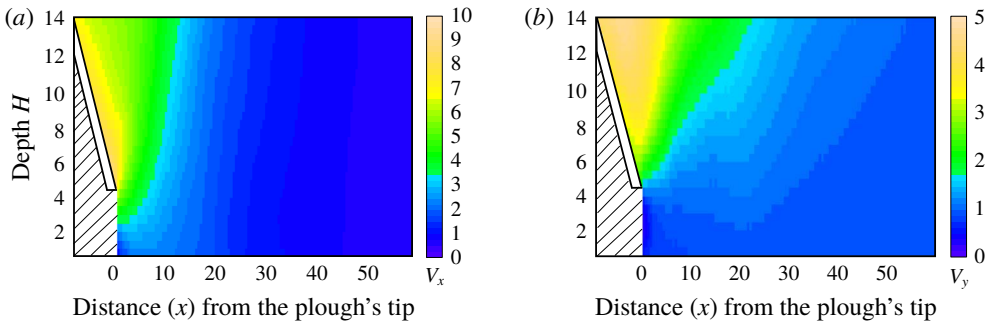


FIGURE 5. (Colour online) Continuum velocity field associated with the granular material for a plough moving with non-dimensional speed $v_c = 10$. (a) Horizontal velocity component V_x . (b) Vertical velocity component V_y . We do not report information in the hatched area.

velocity field data over time to reduce randomness. In a developing flow, the transient time range is divided into finite time windows, over which time averaging is then performed. We have seen that the size of the time window should, at least, be equal to the time it takes the plough to cover a distance of 15 grain diameters in order to remove the randomness in the velocities. An example of a computed velocity field is shown in figure 5. The velocity field that we compute resembles that found by Murthy *et al.* (2013, figure 3) in their preliminary experiments on a vertical plough.

Henceforth, we will work with the continuum velocity field \mathbf{V} rather than with the velocity of individual grains.

4.2. Strains

In a continuum description, let $\mathbf{V} = V_x \hat{\mathbf{i}} + V_y \hat{\mathbf{j}}$ be the velocity of a material point at a point $\mathbf{X} = x \hat{\mathbf{i}} + y \hat{\mathbf{j}}$ in the reference frame of the plough. The velocity gradient tensor is given by

$$\mathbf{L} = \frac{\partial \mathbf{V}}{\partial \mathbf{X}}. \tag{4.3}$$

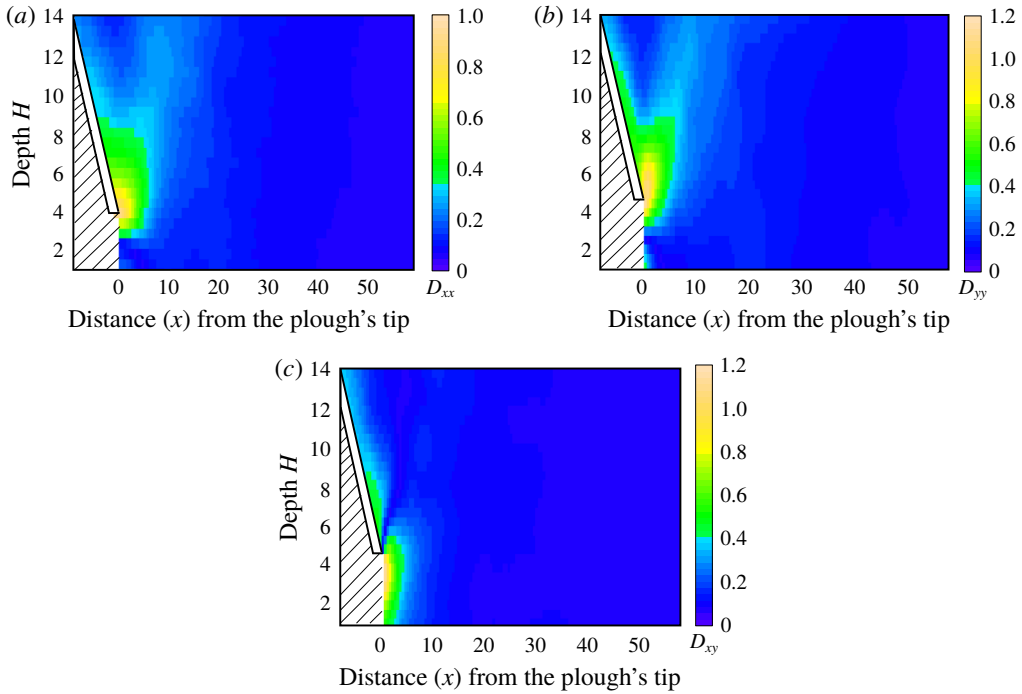


FIGURE 6. (Colour online) Different components of the strain rate tensor \mathbf{D} : (a) normal strain rate D_{xx} ; (b) normal strain rate D_{yy} ; (c) shear strain rate D_{xy} . The plough's non-dimensional speed $v_c = 10$. We do not report information in the hatched area.

For numerically differentiating the velocity field, as in (4.3), the velocity data are further smoothened by using cubic smoothing splines. The smooth.spline function of the 'stats' package in the software R (R Core Team 2013) is employed for this task. The smoothening of the spline fitting is controlled by the parameter spar, with $spar = 0$ corresponding to an interpolating spline with no smoothening, and $spar = 1$ implying a linear least squares fit. After some iterations, we found that $spar = 0.6$ leads to a good fit and gets rid of unwanted fluctuations in the data. Spatial derivatives are then computed numerically. In this context, we note that we have ensured that the grid size that we employ provides an accurate estimate of the strain rates, and this is discussed in appendix A.

The symmetric part of the velocity gradient tensor provides the stretching rate tensor:

$$\mathbf{D} = \frac{1}{2}(\mathbf{L} + \mathbf{L}^T). \tag{4.4}$$

Plots for different components of \mathbf{D} for one instance of ploughing are shown in figure 6. We observe high strain rates near the tip of the plough. This is also evident from the velocity plots in figure 5, where rapid changes in the velocity field are found near the plough's tip.

4.3. Variability with grain properties

The ESPM works best when the system is kinematically controlled, so that grain/system parameters (e.g. inter-grain friction, grain size, ploughing speed) do

not affect the flow significantly. We will gauge the extent to which these parameters affect the strain rate tensor \mathbf{D} by calculating the total average relative error

$$e_{rel}(f; r_i) = \left\{ \frac{\int_{x=0}^l \|\overline{f(x)} - f(x, r_i)\|^2 dx}{\int_{x=0}^l \|\overline{f(x)}\|^2 dx} \right\}^{1/2}, \quad (4.5)$$

where r_i is i th value of a parameter r , with $i = 1 \dots n$, and f is a component of \mathbf{D} , and

$$\overline{f(x)} = \frac{\sum_{i=1}^n f(x, r_i)}{n} \quad (4.6)$$

is the average of f over all r_i at a given location x . We now test to what extent this assumption holds in the context of ploughing.

4.3.1. Grain shape

Grain shape is important in DE simulations because circular grains undergo excessive rotation. Various attempts have been made to include shape effects in DE simulations. For example, Pawar (2013) included rolling resistance between contacting grains, Coetzee & Els (2009) utilized compound grains and Obermayr *et al.* (2011) employed non-rotating grains. We performed simulations using both rotating and non-rotating grains, and found that restricting grain rotations did not have any significant effect on the strain rates in most of the region of interest; see figure 7. However, as shown in figure 7(c), near the plough's surface the relative difference in shear strains became somewhat prominent. This is expected, because non-rotating grains undergo significant slipping at the surface of the plough, whereas rotating grains accommodate shear easily by rotating. However, we see from figure 8, that grains undergo rotations only near the plough and, elsewhere, grain rotations are negligible.

Subsequently, we will perform DE simulations employing non-rotating grains. There are three reasons for this choice. First, we will in §5 estimate stresses from strain fields through a simple constitutive law which does not include the effects of grain rotation. Thus, a consistent formulation requires that we ignore grain rotation in our simulations. Constitutive laws for granular materials that include grain rotation are complex and, perhaps, unwarranted at present. Second, the excess rotation at the plough's surface in figure 8 depends on how a flat-faced plough is modelled in DE simulations. We approximate a flat-faced plough by an array of grains that are bonded together and have half the diameter of the larger grains in the bulk; see inset of figure 3. Reducing the diameter of these grains lowers the extent of grain rotation near the plough, thereby bringing DE simulations with non-rotating grains closer to those wherein the grains are free to rotate. Third, Obermayr *et al.* (2011) have shown that realistic forces on flat-faced ploughs may be obtained from calibrated DE simulations in which grain rotation is prevented. We too will show in §6 that proceeding with non-rotating grains gives us a good match with experiments.

Finally, a general remark. Figure 7 shows that small, negative shear strain rates are seen near the plough. This runs counter to our expectations of a large, positive shear rate when the tool angle α is not shallow. This anomaly is explained by realizing that the x - y coordinate system, in which the components of the strain rate tensor are evaluated and displayed in figure 7, is not aligned with the normal (n) and tangent (t) directions of the plough. When the strain rate components are expressed in the n - t system, we do indeed find a large and positive shear strain rate next to the plough's surface (see figure 9).

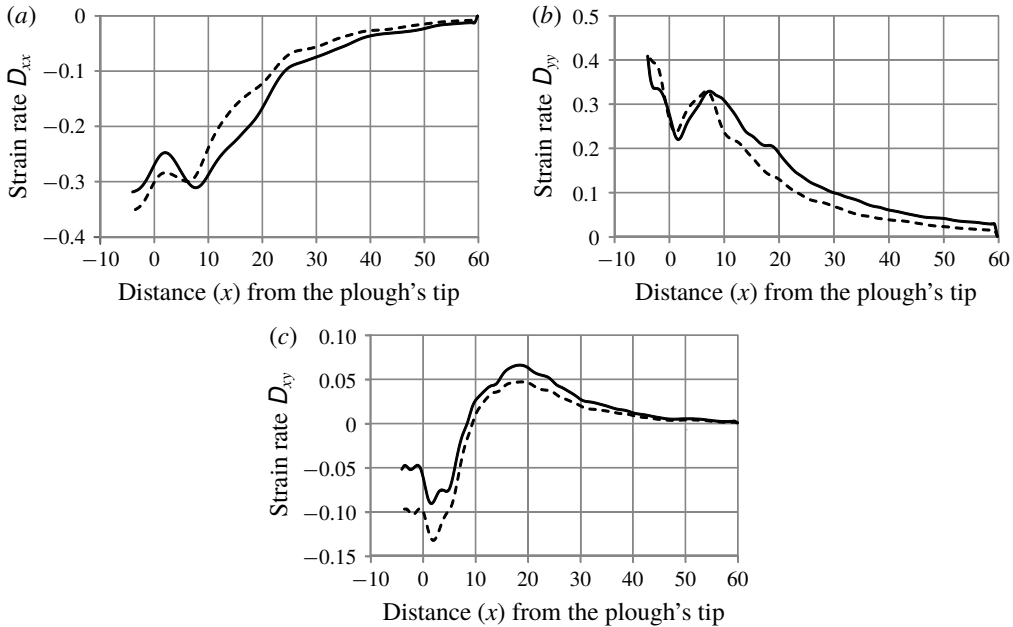


FIGURE 7. Components of the strain rate tensor at points along the line $y = 9$ when rotating grains (solid lines) and non-rotating grains (dashed lines) are implemented. The plough's tip is at $x = 0$. (a) Normal strain rate D_{xx} . (b) Normal strain rate D_{yy} . (c) Shear strain rate D_{xy} . The plough's non-dimensional speed $v_c = 10$, the inter-grain friction $\mu = 0.5$ and grain diameter $d = 0.67$.

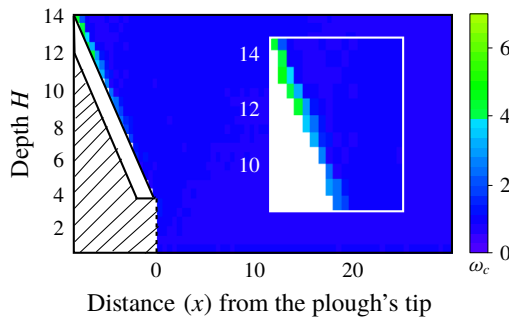


FIGURE 8. (Colour online) The rotation rate ω_c of grains. The rotation rate is nearly zero at most places. The plough's non-dimensional speed $v_c = 10$. We do not report information in the hatched area. Inset shows the higher strain rates near the plough.

4.3.2. Inter-grain friction

Internal friction is the most important (bulk) constitutive property for a cohesionless granular material. Simulations were carried out for values of inter-grain friction μ ranging from 0.1 to 1. The bulk internal friction angle is expected to grow with increasing μ . Figure 10 shows the components of the stretching rate tensor \mathbf{D} along the horizontal line $y = 9$ for different values of μ . The variation in normal strain rates is observed to be within 20% of their mean value, while shear strain rates are

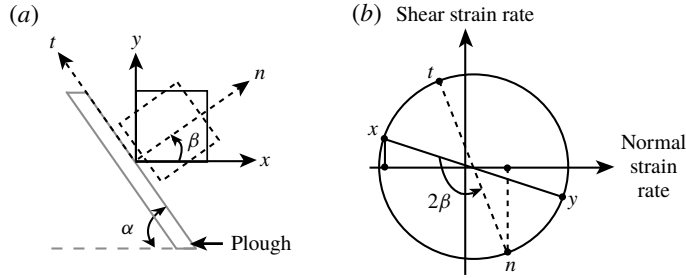


FIGURE 9. (a) Schematic of continuum elements next to the plough's surface in x - y and n - t coordinate systems. (b) Mohr's circle transformation to find strain rates in the n - t system. The angle $\beta = 90^\circ - \alpha$, where $\alpha = 50^\circ$ is the tool angle in our simulations, and D_n and D_t represent normal and shear strain rates, respectively. In our sign convention, a negative ordinate at the x or n points indicates a positive shear strain rate (Crandall, Dahl & Dill 1960).

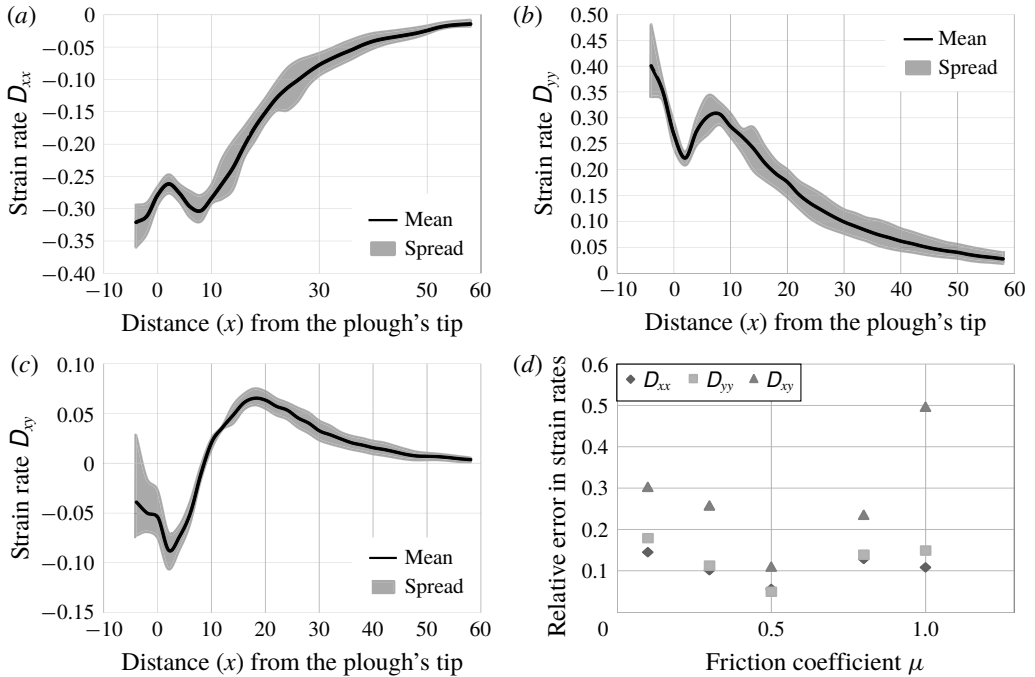


FIGURE 10. The mean value (black line) and spread about the mean (grey region) of the components of the strain rate tensor \mathbf{D} at points along the line $y=9$ for several values of inter-grain friction μ between 0.1 and 1. The plough's tip is at $x=0$. (a) Normal strain rate D_{xx} . (b) Normal strain rate D_{yy} . (c) Shear strain rate D_{xy} . (d) Average relative error in components of the strain rate. The plough's non-dimensional speed $v_c = 10$.

within 30%, except for when $\mu = 1$. We proceed by assuming that strain rates may be considered independent of inter-grain friction.

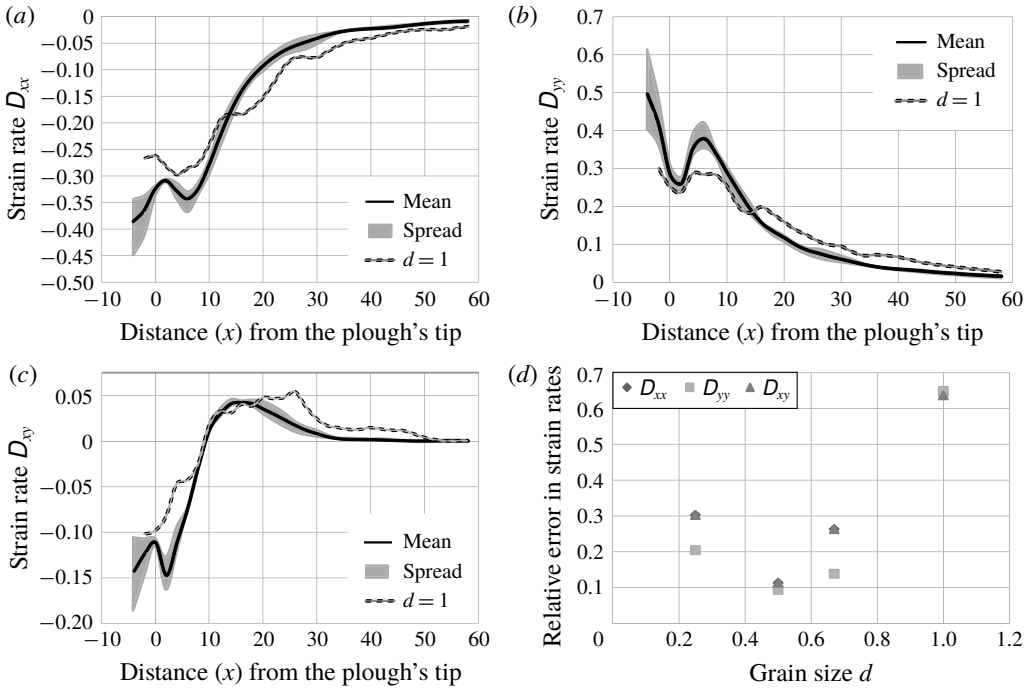


FIGURE 11. The mean value (black line) and spread about the mean (grey region) of the components of the strain rate tensor \mathbf{D} at points along the line $y=9$ for several grain diameters d between 0.25 and 0.67. The strain rates for $d=1$ are shown separately. The number of grains correspondingly reduced from 64 000 to 4000. (a) Normal strain rate D_{xx} . (b) Normal strain rate D_{yy} . (c) Shear strain rate D_{xy} . (d) Average relative error in component of strain rate. The plough's non-dimensional speed $v_c = 10$.

4.3.3. Grain size

Simulations were performed for large grain diameters d of 1, 0.67, 0.5 and 0.25. The ratio of large to small grain diameter was maintained at 1:0.7. As figure 11 shows, there is a drastic change in strain rates when grain size d is decreased from 1 to 0.67. However, further decrease in grain size d causes the strain rates to saturate. Therefore, d is taken to be 0.67 or less in our simulations.

4.3.4. Polydispersity

Simulations were carried out for various mixing ratios of differently sized grains. Again, different polydispersities did not have any significant effect on strain rates. Monodisperse granular beds, however, produced different results because of regular lattice formation. Thus, polydispersity of 10% is maintained in our simulations, as it was enough to avoid lattice formation.

4.3.5. Contact stiffness

Strain rates saturate for values of non-dimensional normal contact stiffness k_n greater than 10^6 . Moreover, in the case of frictional particles, Tripathi & Khakhar (2010) reported that the effect of contact stiffness on granular flow is small once $k_n \geq 2 \times 10^5$. Thus, k_n is taken to be 10^6 in DE simulations. Most naturally occurring grains have values of stiffness much greater than 10^6 , so our approach is consistent.

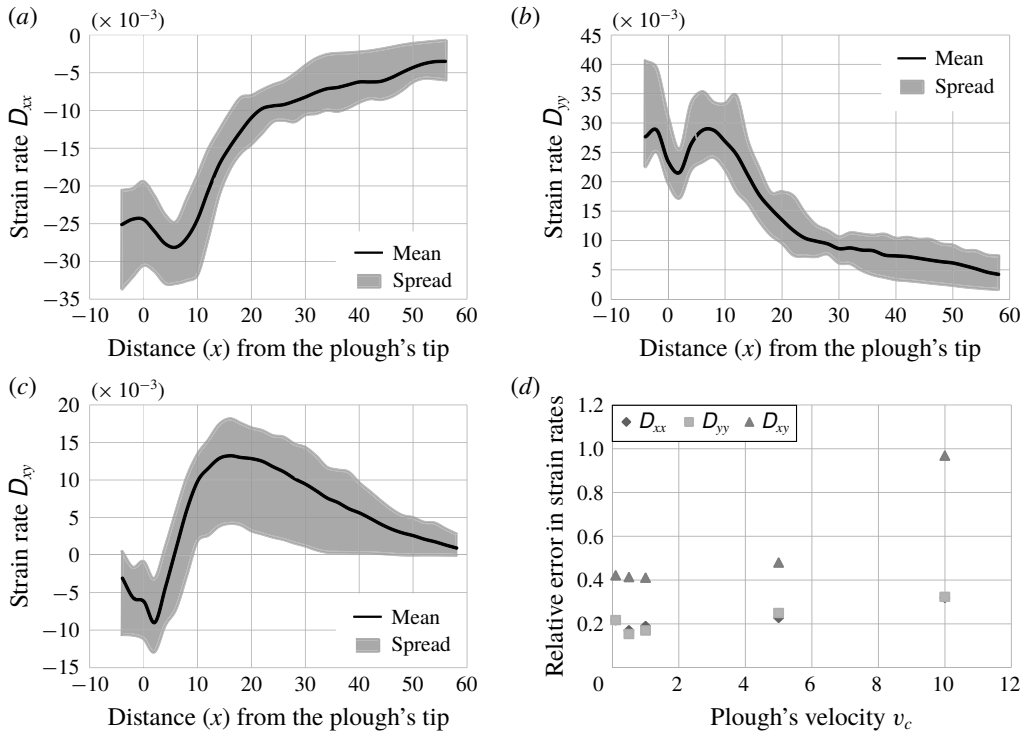


FIGURE 12. The mean value (black line) and the spread about the mean (grey region) of the components of the strain rate tensor \mathbf{D} along the line $y=9$ for five different ploughing velocities v_c between 0.1 and 10. (a) Normal strain rate D_{xx} . (b) Normal strain rate D_{yy} . (c) Shear strain rate D_{xy} . (d) Average relative error in component of strain rate. The inter-grain friction $\mu = 0.5$ and grain diameter $d = 0.67$.

4.3.6. Ploughing speed

Strain rates do change with ploughing speed. This is also in agreement with Percier *et al.* (2011). Strain rates for different ploughing speeds are plotted in figure 12. At smaller velocities, deformations get time to propagate to larger distances, whereas at larger velocities deformations are unable to reach that far. The non-dimensional velocities in figure 12 vary from 0.1 to 20 which corresponds to the range 0.8–16 m s⁻¹ when inter-grain friction $\mu = 0.5$ and grain diameter $d = 0.67$. Therefore, incorporating the correct ploughing speed in the simulations is necessary for accurate prediction of strain rates.

5. Continuum model

5.1. Rheology

We now develop a continuum description for the flowing granular material. This will help find stresses in the bulk when combined with strain rates found from DE simulations.

The transition during ploughing from initial solid-like granular bed to a flowing material requires an appropriate constitutive model. We model the granular bed as a

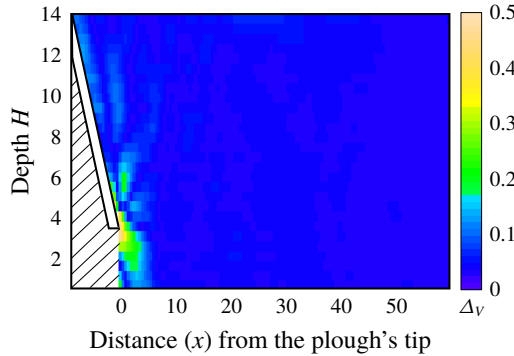


FIGURE 13. (Colour online) Time-averaged dilatation Δ_v . The plough's non-dimensional speed $v_c = 10$. We do not report information in the hatched area.

pressure-dependent Bingham fluid in which both yield stress and friction during flow depend on the local pressure. The Bingham fluid remains rigid until the stress state violates a yield condition and begins to flow post-yield. We assume for simplicity that the flow post-yield preserves volume. To verify this assumption, we find the dilatation as the trace of the strain rate field estimated from our DE simulations. The result is shown in figure 13 and we observe that, to a great extent, the volume in the bulk does remain preserved. The maximum dilatation is found at the tip of the plough. However, we do not expect accurate estimation of dilatation to have a significant bearing upon the forces exerted on the plough, and this expectation has been endorsed by Coetzee (2014) through detailed discrete and continuum simulations.

Sharma (2017, § 2.10.1) shows that the post-yield stress in the granular bed when modelled as above is

$$\boldsymbol{\sigma} = -p\mathbf{1} + kp \frac{\mathbf{D}}{|\mathbf{D}|}, \tag{5.1}$$

where the pressure

$$p = -\frac{1}{3} \text{tr } \boldsymbol{\sigma}, \tag{5.2}$$

the parameter

$$k = \frac{2\sqrt{6} \sin \varphi}{3 - \sin \varphi} \tag{5.3}$$

in terms of the soil's internal friction angle φ and, in indicial notation, $|\mathbf{D}|^2 = D_{ij}D_{ij}$. Thus, knowing the strain rate \mathbf{D} and pressure p will allow us to compute the stress $\boldsymbol{\sigma}$. We estimate the pressure p in the next section.

The constitutive law (5.1) has been employed to model flowing grains in the past (e.g. Schaeffer 1987; Sharma 2017). The law (5.1) is very similar to the rheology proposed by Jop *et al.* (2006) with the key difference being that here k replaces the friction coefficient $\mu(I)$ of Jop *et al.* (2006), which is a function of the inertial number I . The parameter k depends on the granular material only through its macroscopic friction angle φ that, in turn, is related to the properties of the constituent grain, but not on the flow rate. The friction coefficient μ , on the other hand, is also affected by the flow rate through the inertial number.

We make the following regarding our choice of the constitutive law. Recent research (Barker *et al.* 2015) has shown that the $\mu(I)$ -rheology is well-posed for intermediate values of I , but not for all I . The same could be true for the material model (5.1). To this end, we note the following:

- (i) Because we do not integrate in time, the ill-posedness will not affect ESPM. Mathematically ill-posed problems suffer from unbounded growth of short-wavelength perturbations, which necessarily leads to grid-dependent numerical results that do not converge as the spatial resolution is enhanced. Thus, the ill-posedness of the constitutive law becomes crucial when numerically integrating the temporal dynamics of a system. Schaeffer and co-workers (Pitman & Schaeffer 1987; Schaeffer 1987; Schaeffer & Pitman 1988; Thomas & Schaeffer 1988; Schaeffer 1990; Metcalfe *et al.* 2002) studied the time evolution of two- and three-dimensional, incompressible granular and plastic flows. They stated the conditions under which the governing equations become unstable and ill-posed. They considered the Tresca and von Mises yield criterion; it is unknown whether the Drucker–Prager yield criterion that we employ displays the same behaviour. However, in ESPM, the dynamics of the granular material is evolved temporally through DE simulations, not by the numerical integration of the governing continuum equations. The DE simulations provide the velocity data of the grains at any given instant of time. At that given, fixed instant, the velocity data are spatially smoothed to obtain the continuum velocity and strain fields in the granular material. From these continuum fields the stresses everywhere in the granular material, at that given time, are found by invoking an appropriate constitutive law. Thus, the equations governing the dynamics of the granular material in a continuum description are never numerically integrated. As a result, the possible ill-posedness of the constitutive law (5.1) does not, in any way, affect the final results.
- (ii) More importantly, ESPM is agnostic to the choice of the constitutive law, and we are free to utilize more specific and/or sophisticated ones, as per our requirements. We prefer to go with the law (5.1) because it is simple, popular, gives reasonable results and serves the purpose of demonstrating ESPM without getting the discussion mired in the complexity of detailed rheological modelling of granular flows.

In closing, it is important to emphasize that the material model is not tuned to a specific application, which would not be the case if we were to calibrate the grain parameters in our DE simulations.

5.2. Pressure

The linear momentum balances in the x and y directions are, respectively,

$$\frac{\partial \sigma_{xx}}{\partial x} + \frac{\partial \sigma_{xy}}{\partial y} = \rho a_x \quad (5.4)$$

and

$$\frac{\partial \sigma_{xy}}{\partial x} + \frac{\partial \sigma_{yy}}{\partial y} = \rho(a_y + g), \quad (5.5)$$

where a_x and a_y are the x and y components of the acceleration field \mathbf{a} obtained from (4.2), g is the acceleration due to gravity and ρ is the bulk density. Substituting (5.1) into the the above and eliminating $\partial p/\partial y$, we obtain

$$\begin{aligned} \frac{\partial p}{\partial x} & \left\{ \left(k \frac{D_{xx}}{|\mathbf{D}|} - 1 \right) \left(1 - k \frac{D_{yy}}{|\mathbf{D}|} \right) + k^2 \left(\frac{D_{xy}}{|\mathbf{D}|} \right)^2 \right\} + k^2 p \left\{ \frac{\partial}{\partial y} \left(\frac{D_{yy}}{|\mathbf{D}|} \right) + \frac{\partial}{\partial x} \left(\frac{D_{xy}}{|\mathbf{D}|} \right) \right\} \frac{D_{xy}}{|\mathbf{D}|} \\ & + kp \left\{ \frac{\partial}{\partial x} \left(\frac{D_{xx}}{|\mathbf{D}|} \right) + \frac{\partial}{\partial y} \left(\frac{D_{xy}}{|\mathbf{D}|} \right) \right\} \left(1 - k \frac{D_{yy}}{|\mathbf{D}|} \right) \\ & = \rho a_x \left(1 - k \frac{D_{yy}}{|\mathbf{D}|} \right) + k \rho \frac{D_{xy}}{|\mathbf{D}|} (a_y + g). \end{aligned} \tag{5.6}$$

The strain rates, acceleration and density are known from the continuum kinematic fields obtained from DE simulations and the rheology assumed in § 5.1. Thus, the above equation may now be integrated to find the pressure p . This we discuss next.

5.2.1. Integration scheme

The pressure p at a fixed depth y may be found by integrating (5.6) with respect to x over the region that has yielded and is flowing. In a Bingham fluid, we need to distinguish between unyielded and flowing regions. The post-yield rheology (5.1) and the differential equation (5.6) for the pressure p are applicable only in the flowing region.

We thus need to find the extent of the flowing region. Distinction between unyielded and flowing regions may be made on the basis of strain rates, e.g. through $|\mathbf{D}|$, which is a measure of the extent of flow. In the unyielded region $|\mathbf{D}|$ should, theoretically, be zero. In figure 14(a), $|\mathbf{D}|$ is plotted as a function of the distance from the plough for different depths. We see that $|\mathbf{D}|$ far away from the plough stays nearly zero, but increases sharply as we move towards the plough. In granular materials forces travel through force chains (Liu *et al.* 1995), so that small fluctuations are always present, which causes small non-zero values of $|\mathbf{D}|$ to be found even in far away regions where the granular material, for all practical purposes, has still not yielded. We therefore define a critical value $|\mathbf{D}|_c$ and material with $|\mathbf{D}| > |\mathbf{D}|_c$ is said to be flowing, else it has not yielded. We set $|\mathbf{D}|_c = \beta |\mathbf{D}|_{max}$, where $|\mathbf{D}|_{max}$ is the maximum observed value of $|\mathbf{D}|$ at a given ploughing speed. A plot with $\beta = 0.05$ showing the variation of $|\mathbf{D}|$ is shown in figure 14(b). The region to the left of the boundary $|\mathbf{D}| = |\mathbf{D}|_c$ is flowing while the right-hand side region is, as yet, unyielded.

The effect of the choice of $|\mathbf{D}|_c$ on horizontal force calculations (discussed below) is shown in figure 15. We see that the horizontal force is relatively insensitive to the choice of β between 5% and 10%. For $\beta < 5\%$, the unyielded region expands and begins affecting the force calculation, as observed by the sudden increase in the horizontal force in figure 15. With β more than 10%, the force starts decreasing rapidly, which indicates that we are allowing the region identified as unyielded to encroach into a region where material is, in fact, flowing. Thus, we set $\beta = 0.05$.

To find the pressure p we integrate (5.6) numerically from the yield boundary towards the plough along horizontal lines, e.g. the dashed line in figure 14(b), employing the grid constructed in figure 5. Pressure at a point on this boundary is taken to be due to the weight of the granular material above it, i.e. lithostatic. Thus, pressure on the yield boundary is ρgh , where ρ is the bulk density of the granular bed and h is the depth of the point from the free surface (see figure 14b). The height h may be obtained from DE simulations (after appropriate rescaling) or

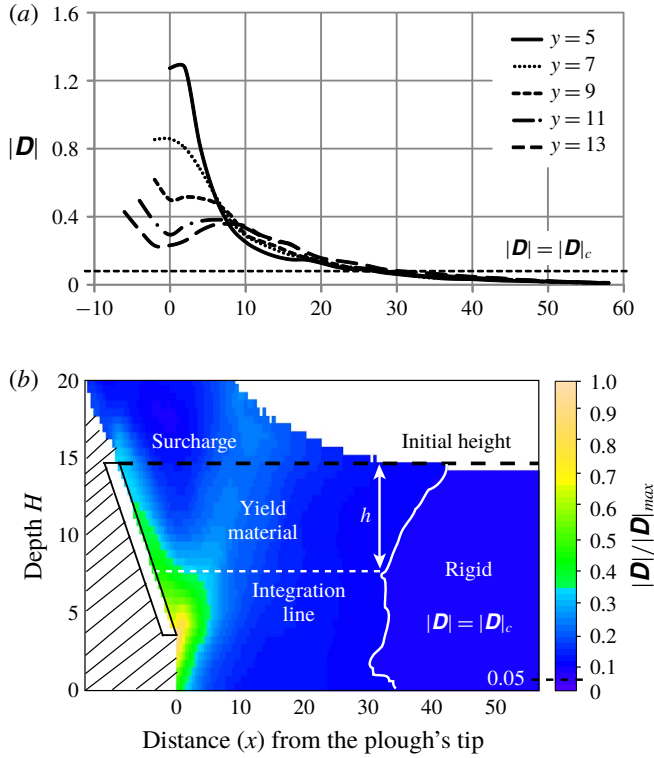


FIGURE 14. (Colour online) Distinguishing between yielded and unyielded regions. (a) The magnitude of the strain rate tensor $|D|$ with distance from tool tip at different depths y . The line $|D| = |D|_c$, with $|D|_c = 0.05|D|_{max}$ is also shown. Here, we find that $|D|_{max} = 1.7$ at $y = 4$ (not shown). (b) The magnitude of strain rate $|D|$ in the entire material. The yielded boundary obtained by setting $|D|_c = 0.05|D|_{max}$ is also shown. The granular material which accumulates above the initial height of the granular bed is defined as the surcharge. The plough's non-dimensional speed $v_c = 10$. We do not report information in the hatched area.

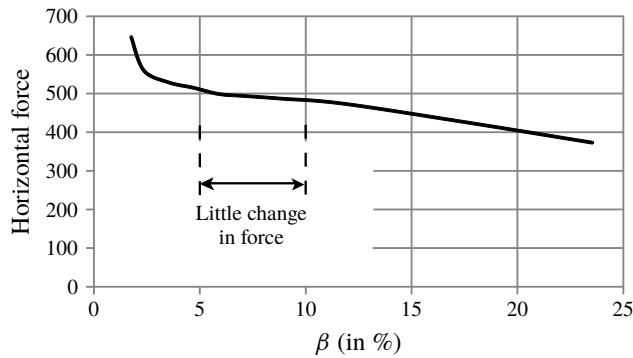


FIGURE 15. Effect of choice of $|D|_c$ on horizontal force on a plough moving with non-dimensional speed $v_c = 5$.

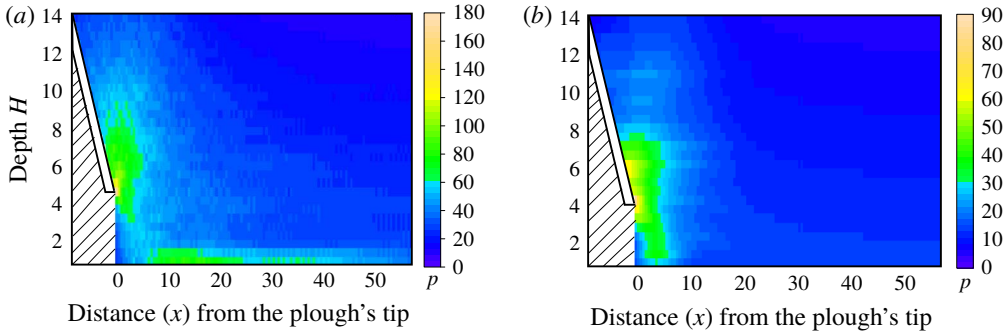


FIGURE 16. (Colour online) Comparison of pressure p in the bulk obtained (a) from DE simulations with $\mu = 0.3$ and (b) by following the procedure of § 5.2 with $\varphi = 25^\circ$. In each case the plough’s non-dimensional speed $v_c = 10$. We do not report information in the hatched area.

from experiments. In (5.6), we know a_x , a_y and \mathbf{D} at the grid points. The terms involving derivatives of \mathbf{D} in (5.6) are calculated using finite differences. Step size for integration is therefore the same as the grid size in figure 5. Integrating (5.6) allows us to estimate the pressure everywhere in the flowing region. We note that the pressure in the rigid and surcharge regions is also taken to be lithostatic.

5.2.2. Comparison

Qualitative validation of the pressure field obtained in the previous section may be obtained by comparing with pressure found directly from our uncalibrated DE simulations. For a quantitative match, it is necessary to tune the grain properties employed in our DE simulations to the bulk internal friction angle employed in our continuum model, which has not been done. In the literature, available calibrated grain data are for three-dimensional ploughing (e.g. Obermayr *et al.* 2011), while ours is a two-dimensional system.

The average pressure on grain i may be found from a DE simulation by (e.g. Bhatija *et al.* 2016)

$$p_i = \frac{1}{S_i} \sum_j f_{ij}^n, \tag{5.7}$$

where f_{ij}^n is the normal force exerted upon grain i by grain j that abuts grain i and S_i is the surface area of the i th grain. This average pressure is calculated for every grain at every time step and then averaged over space and time to, finally, provide the pressure field. Figure 16(a) shows the pressure variation obtained directly from our uncalibrated DE simulation. We find a good qualitative match with the continuum pressure field in figure 16(b) that is obtained by solving (5.6). Both figures predict that a high-pressure region develops near the tip of the plough.

In passing, we note that in figure 16(a) a high-pressure region is seen at the bottom of the granular bed in DE simulations, but not in the continuum pressure field estimated by ESPM. We believe that this is because the flow field is not well resolved near the channel’s base.

5.3. Forces

Once pressure is known everywhere, equation (5.1) allows us to find normal and shear stress everywhere in the plastic region. The normal force F_N on the tool's surface (see figure 1) may then be estimated by integrating the normal stress component σ_{nn} over its surface:

$$F_N = \int_{S_t} \sigma_{nn} dA, \quad (5.8)$$

where S_t is the surface area of the plough in contact with the granular material. The normal stress component is related to stress components in the x - y coordinate system (see figure 1) by

$$\sigma_{nn} = \frac{1}{2}(\sigma_{xx} + \sigma_{yy}) - \frac{1}{2}(\sigma_{xx} - \sigma_{yy}) \cos 2\alpha + \sigma_{xy} \sin 2\alpha, \quad (5.9)$$

which follows from the Mohr circle, and where α is the inclination of the plough. Similarly, from the Mohr circle, the shear stress component

$$\sigma_{nt} = -\frac{1}{2}(\sigma_{xx} - \sigma_{yy}) \sin 2\alpha + \sigma_{xy} \cos 2\alpha, \quad (5.10)$$

which provides the total shear force on the tool as

$$F_T = \int_{S_t} \sigma_{nt} dA. \quad (5.11)$$

Knowledge of F_N and F_T allows us to compute horizontal and vertical forces on the plough in a straightforward manner.

6. Results and discussion

As a preliminary exercise to build confidence in ESPM in the context of a well-studied granular system, we have utilized ESPM to investigate granular flow down an inclined plane. We find an excellent match with theoretical predictions predicated upon the $\mu(I)$ -rheology (Jop *et al.* 2006; Pouliquen & Forterre 2009), and this is discussed in detail in appendix B. Here we proceed to compare the ploughing forces predicted by ESPM against those measured in experiments and estimated by calibrated DE simulations.

6.1. Calibrated DE simulations

Obermayr *et al.* (2011) carried out three-dimensional simulations and experiments with steel balls and gravel, in which a vertical plate cuts through a granular bed. The internal friction angles measured experimentally from triaxial compression tests were $\varphi = 21.3^\circ$ for steel balls and $\varphi = 30^\circ$ for gravel. The parameters of their DE simulations were calibrated by matching them with triaxial tests. Consequently, the microscopic inter-grain friction to be utilized in DE simulations was determined to be $\mu = 0.07$ for steel balls and $\mu = 0.3$ for gravel. Obermayr *et al.* restricted grain rotations in their DE simulations.

In this section, we will compare the predictions for ploughing forces obtained from ESPM with those of calibrated DE simulations. To this end, we take the calibrated data from Obermayr *et al.* (2011) and perform two separate sets of DE simulations of two-dimensional ploughing: one with $\mu = 0.07$ to model steel balls and the other with $\mu = 0.3$ for gravel. Corresponding to these two DE simulations, we set the

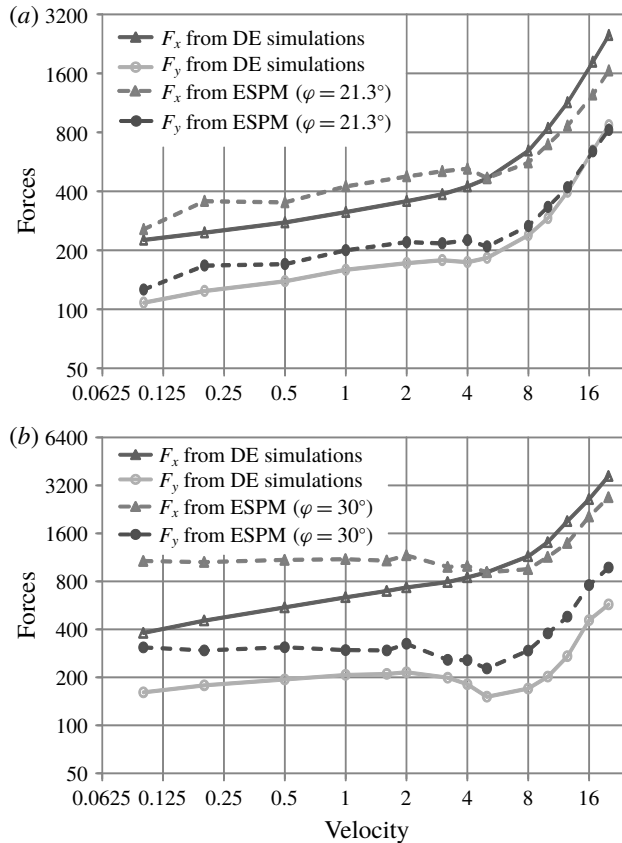


FIGURE 17. Comparison of ploughing forces computed from ESPM and DE simulations. Here, F_x and F_y represent the horizontal and the vertical forces on the plough, respectively. (a) Steel balls. ESPM: $\varphi = 21.3^\circ$; DE simulations: $\mu = 0.07$. (b) Gravel. ESPM: $\varphi = 30^\circ$; DE simulations: $\mu = 0.3$.

bulk internal friction angles in our ESPM calculations as, respectively, $\varphi = 21.3^\circ$ and $\varphi = 30^\circ$. Simulations are now performed for a plough with angle $\alpha = 50^\circ$ over a range of ploughing speeds utilizing the preceding two values of φ ; this is supposed to imitate ploughing of steel and gravel, respectively. Because we are employing calibrated data, it may be expected that forces computed by our DE simulations should match ESPM predictions. However, we note a major difference between our DE simulations and those of Obermayr *et al.*: the latter were three-dimensional simulations with spherical grains, while we restrict ourselves to two dimensions with disc-shaped grains. Thus, the calibrated microscopic inter-grain friction obtained by Obermayr *et al.* may not be applicable to our two-dimensional system.

In figure 17, horizontal and vertical forces computed directly from our DE simulations (with calibrated data from Obermayr *et al.*) are compared with forces obtained from ESPM. The ESPM curves show good qualitative match with simulations, but some quantitative deviations are observed, e.g. gravel in figure 17(b). We believe that the quantitative mismatch is due to our using calibrated data from Obermayr *et al.* (2011), obtained originally for three-dimensional simulations, in our two-dimensional DE simulations. Furthermore, we assumed a simple rheological

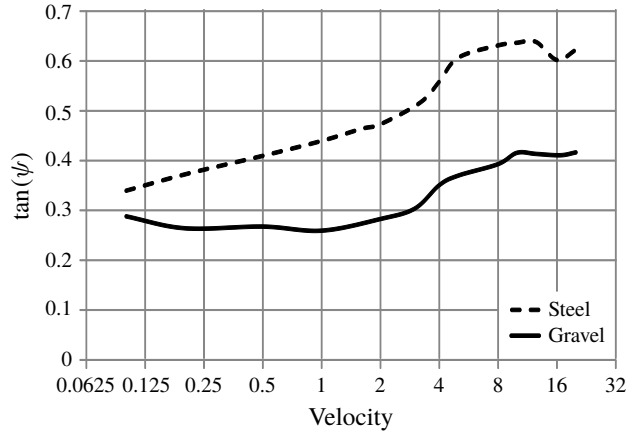


FIGURE 18. Variation of ψ defined in (6.1) with ploughing velocity for simulations with steel ($\mu = 0.07$) and gravel ($\mu = 0.3$).

model in our ESPM calculations. We expect that employing grain data correctly calibrated for a two-dimensional system, along with a more detailed rheology will provide a closer match.

We now report an interesting observation. Predictions from ESPM are greatly improved if, instead of using the experimentally measured internal friction angle in ESPM computations, we set the friction angle $\phi = \psi$ in (5.3), where

$$\tan \psi = \frac{F_N}{F_T} \quad (6.1)$$

is the plough-grain friction angle found from the normal (F_N) and tangential (F_T) forces computed from our two-dimensional DE simulations, which employed the calibrated data of Obermayr *et al.* (2011). We first note from figure 18 that ψ varies with ploughing speed for both steel and gravel, and we incorporate this variation into ESPM. When this is done, the match with forces predicted from DE simulations improves significantly in the low-velocity regime (see figure 19). However, the disadvantage of this modification is that we need calibrated DE parameters to obtain ψ , which undermines the fundamental advantage of ESPM in that it avoids calibration of DE parameters.

6.1.1. Variation with ploughing speed

There are two ways in which kinetic energy input to the plough is lost: (i) frictional dissipation in the soil and (ii) momentum transfer to soil (inertial effects). In figure 17, a marked change in the curves may be observed around $v_c \approx 5$; forces increase sharply from this point onwards. This change may be explained as follows. The frictional force is proportional to the pressure in the bulk, which may be estimated to be ρgh , and the inertial force is proportional to $\rho v_c^2/2$. Inertial effects are negligible at low velocities. They become relevant only when they become comparable to frictional forces, i.e. when $\rho gh/0.5\rho v_c^2 \approx 1$, which gives $v_c \approx \sqrt{2gh} \approx 5.5$, where h in the DE simulations was about 15 particle diameters. Thus, the change in the curves in figure 17 at $v_c \approx 5$ may be understood in terms of the increasing contribution of inertial effects in comparison to frictional resistance. Both DE simulations and ESPM successfully capture this feature.

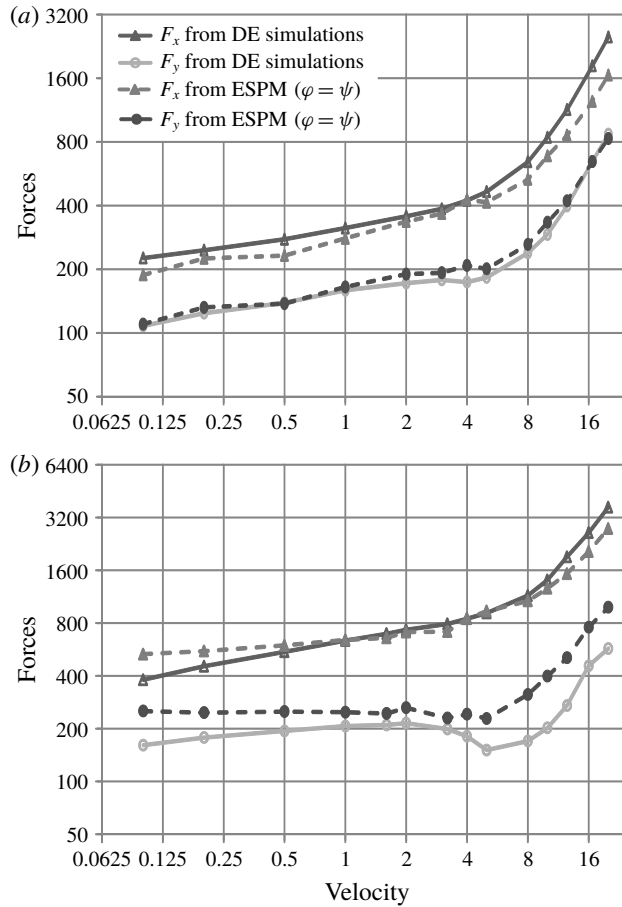


FIGURE 19. Comparison of ploughing forces computed from ESPM with $\varphi = \psi$ in (5.3) with ψ found from (6.1), and DE simulations. Here, F_x and F_y represent the horizontal and the vertical forces on the plough, respectively. (a) Steel balls. DE simulations: $\mu = 0.07$. (b) Gravel. DE simulations: $\mu = 0.3$.

6.2. Experiments

6.2.1. Corn grains

Coetzee & Els (2009) performed experiments and two-dimensional DE simulations for a vertical plough cutting through a bed of corn grains. In their experiments: the vertical plough had an initial depth of 200 mm and width of 200 mm; the measured internal friction angle was 23° ; the calibrated microscopic grain properties yielded a grain density of 855 kg m^{-3} , inter-grain friction coefficient μ_p of 0.12 and contact spring stiffness k_n of 450 kN m^{-1} . Coetzee & Els (2009) used calibrated data in their DE simulations.

To apply ESPM we performed DE simulations using uncalibrated data shown in table 1, with grain friction coefficient $\mu = 0.12$. Another major difference between the DE simulations of Coetzee and Els and ours is that the former used clumped grains to imitate the shape of the corn grains, whereas we employ non-rotating, disc-shaped grains. The differences in the two DE simulations are reflected in figure 20, where we

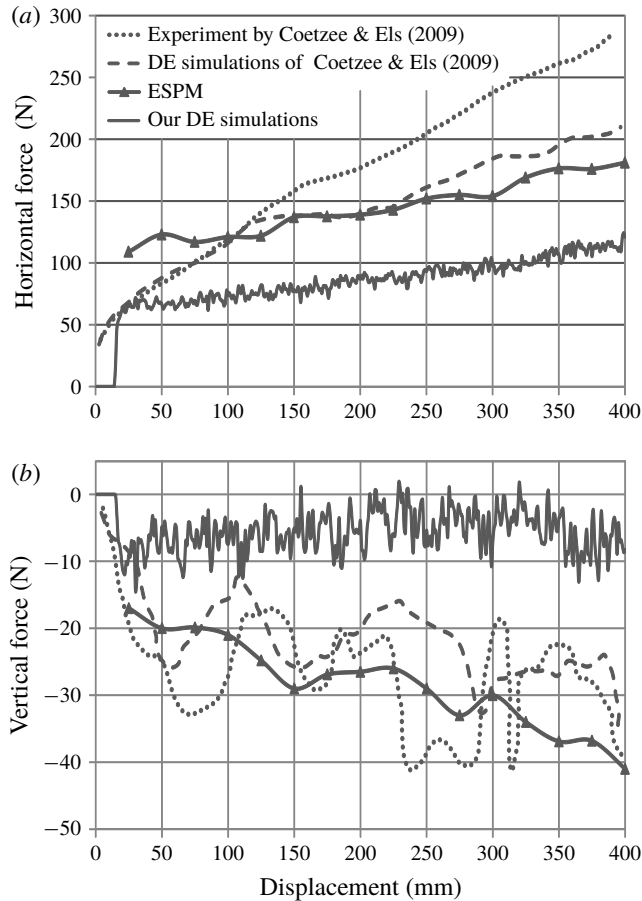


FIGURE 20. Comparing estimates for forces on the plough employed in the experiments of Coetzee & Els (2009). Also shown are results from our two-dimensional simulations and those of Coetzee & Els (2009), as well as predictions of ESPM. (a) Horizontal force. (b) Vertical force. Because the flow is developing, the transient time range is divided into finite time windows over which time averaging is done.

see that the two simulations predict very different ploughing forces. We discuss this further below.

In figure 20, we show the ploughing force measured by Coetzee & Els (2009) in their experiments and computed by their calibrated two-dimensional DE simulations, the predictions of our uncalibrated two-dimensional DE simulations and, finally, the results of two-dimensional ESPM obtained after setting $\varphi = 23^\circ$ to match the bulk internal friction angle measured by Coetzee & Els (2009). We see that ploughing forces predicted from the calibrated two-dimensional DE simulation and our ESPM are less than what is experimentally measured. This is because frictional forces exerted by the side walls in the experiments are not included in both two-dimensional DE simulations and ESPM. However, forces from the ESPM calculation come close to those predicted by calibrated DE simulations. This match is to be expected because the DE simulations of Coetzee & Els (2009) utilized grain data calibrated to match

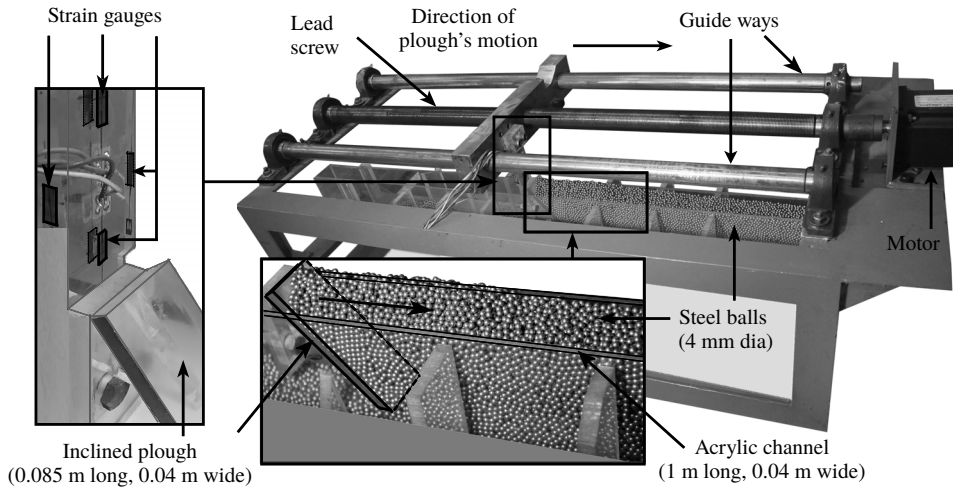


FIGURE 21. Experimental set-up to measure the ploughing force when a rigid, flat, inclined plough moves through a bed of steel balls.

the bulk internal friction angle φ of corn grains, and our ESPM, which employs the rheology of § 5.1, relies only on this choice of φ .

Figure 20 also plots predictions of our uncalibrated two-dimensional DE simulations that provided the kinematic data for our ESPM calculations. Forces predicted directly from our DE simulations, which employed disc-shaped grains, were less than those of all other predictions shown in figure 20, including the calibrated DE simulations of Coetzee & Els (2009). This is because our DE simulations employ circular discs whose frictional properties were not tuned to capture the frictional interaction between corn grains. This underlines the importance of calibrating DE simulations to the actual macro-properties of the soil whenever force data are sought directly from DE simulations.

We saw in § 4.3 that ploughing is strain controlled to a great extent. Strain rates during ploughing are, therefore, largely insensitive to grain properties utilized in DE simulations. Thus, clumped grains employed by Coetzee & Els (2009) in their DE simulations flowed in a manner very similar to our disc-shaped grains. Indeed, the maximum vertical displacement seen in our uncalibrated DE simulations was 142 mm, which is very close to the 145 mm peak displacement found by Coetzee and Els in their calibrated simulations. This explains the agreement of our ESPM calculations with the DE simulations of Coetzee and Els, even though the ESPM calculations utilized the strain field from our uncalibrated DE simulations. The fact that we obtained a good prediction from ESPM (i) without the extensive effort required to tune DE simulations and (ii) while using simple disc-shaped grains rather than the complex clumped grains of Coetzee and Els underscores the main advantages of ESPM.

6.2.2. Steel balls

Finally, we compare ESPM results with our experiments in which a rigid, flat, inclined plough made of acrylic ploughs through a bed of steel balls. The system is shown in figure 21. The length and width of the channel are 1 m and 40 mm, respectively, and the depth of the plough's cut is 70 mm. The bed is a mixture of

steel balls having diameters of either 4 or 3 mm. The inclination angle of the plough is kept at 50° . The plough is mounted with a load cell consisting of strain gauges that are used for measuring horizontal and vertical forces. The lead screw with pitch length of 2 mm is driven by a stepper motor. The plough is attached to the lead screw that travels along two guideways on either side. The plough moves at speeds between 1 and 18 mm s^{-1} . Due to the limitation of the pitch length of the lead screw, we were unable to perform experiments over the entire range of speeds covered by simulations and ESPM. Only a small amount of surcharge accumulates (lower inset of figure 21) as the steel balls spill over the channel's sidewalls. The channel is made of acrylic so that the friction of the walls with the steel balls may be ignored. Finally, we estimated the internal friction angle of an aggregate of steel balls to be 21° by measuring the angle of repose of a heap of steel balls.

Kinematic data were obtained from uncalibrated DE simulations that employed parameters from table 1 and then following the process of §§ 4.1 and 4.2. In ESPM calculations the effective bulk density is taken to be 4830 kg m^{-3} to match the density of steel times the volume fraction of 0.615 observed in DE simulations.

Figure 22 shows a comparison of the experiments with uncalibrated DE simulations and ESPM results. As expected, force predictions from DE simulations do not match experiments well. At the same time, the horizontal force measured from experiments is in good agreement with that predicted by ESPM. The vertical force found from ESPM, however, is higher than that measured in experiments. The absence of surcharge (lower inset of figure 21) and the presence of sidewall friction in our experiments are possible sources of this difference, as we show next.

The vertical force on the plough is affected only by the surcharge. However, the horizontal force is impacted by both the surcharge and the sidewall friction. Consider first the effect of the surcharge. From the universal earth-moving equation (McKyes 1985), the contribution of the surcharge to force normal to the plough is estimated using

$$F_{sur}^n = q_s H N_s w, \quad (6.2)$$

where q_s is the lithostatic surcharge pressure, H is the ploughing depth, N_s is the surcharge factor that depends on the plough's geometry and friction angle of granular material and w is the plough's width. From our DE simulations, the average height of surcharge above the plough is approximately $H/2$ and, hence, surcharge pressure $q_s = \rho g H/2$. The surcharge factor N_s for a plough with inclination angle $\alpha = 50^\circ$ and a granular material with friction angle $\varphi \approx 21^\circ$ is 1.61 (McKyes 1985, App. 1, p. 167). With this, F_{sur}^n is found to be 7.48 N for our experiments. At the same time, the tangential force F_{sur}^t on the plough's surface due to the excess normal force F_{sur}^n is

$$F_{sur}^t = \mu_{as} F_{sur}^n, \quad (6.3)$$

where $\mu_{as} = 0.15$ is the coefficient of dynamic friction between acrylic and dry steel. The corrected experimental measurements for the vertical force on the plough, obtained by adding the vertical components of F_{sur}^n and F_{sur}^t to the experimental values, are also shown in figure 22(a). We now find a good match between experiment and ESPM.

Correcting the experimentally measured horizontal force is more involved. The horizontal force should be first augmented by the horizontal components of F_{sur}^n and F_{sur}^t . At the same time, the contribution of the sidewall friction in experiments needs to be subtracted from the value of the horizontal force measured in experiments. We estimate the frictional force exerted by the sidewalls in our experiments by

$$F_{sw}^t = \mu_{as} P_{sw} A_{sw}, \quad (6.4)$$

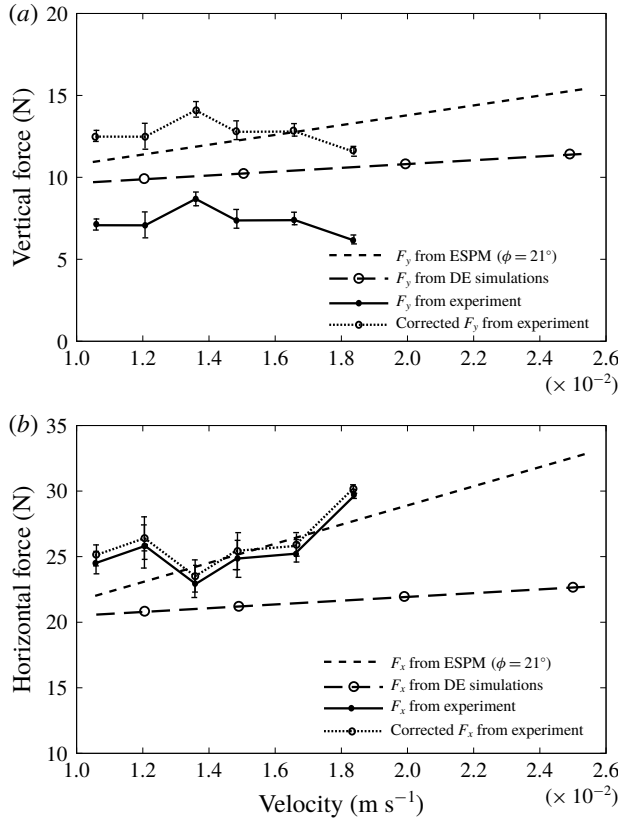


FIGURE 22. Comparison of horizontal and vertical forces on the plough for the experiments of figure 21. (a) Vertical force (F_y). (b) Horizontal force (F_x).

where $A_{sw} = l_f H$ is the sidewall area over which the friction force acts and P_{sw} is the normal traction exerted by the grains on the sidewall. The traction P_{sw} is estimated by

$$P_{sw} = K_0 F_H / A_{cs}, \tag{6.5}$$

where the at-rest earth pressure coefficient $K_0 = (1 - \sin \phi) \approx 0.64$ (McKyes 1985), $A_{cs} = Hw$ is the cross-sectional area of the channel and F_H is the measured horizontal force. The length l_f over which the sidewall friction is mobilized is considered to be of the order of plough's width $w = 0.04$ m. This estimate is also consistent with the experiments of Tanaka *et al.* (2000) and Asaf *et al.* (2007) which had plough velocities in the same range as in our experiments. The corrected horizontal force is plotted using dashed lines in figure 22(b), and is observed to be slightly higher than the value originally measured. The good agreement between experiments and ESPM nevertheless persists.

Finally, we note that in our ESPM computations we have ignored the contribution of frictional interaction between the granular flow and the aft side of the plough. This is because (i) we expect the normal force exerted by the grains on the aft side of the plough to be small, given that the granular flow has a free surface just beyond the plough, i.e. for $x < 0$, and (ii) the plough's thickness is small.

7. Conclusions

The main objective of the paper was to demonstrate that we can calculate forces during ploughing of a granular bed by combining a continuum model of the granular flow with kinematic information obtained from uncalibrated DE simulations. Discrete element simulations can yield reliable force data only if they are first calibrated and if the number of grains is large enough. Calibration requires significant effort and is often system specific. Our method, which we label as the ESPM, obviates the need to calibrate DE simulations and also required far fewer grains.

The ESPM is useful for granular flows that are strain controlled, i.e. the strain field in the granular medium remains largely independent of grain properties such as shape, size and surface roughness. To this end we probed through DE simulations the extent to which ploughing is strain controlled and concluded that, for small enough grains, ploughing is strain controlled to a fair approximation. This allowed us to compute the strain field from coarse, uncalibrated, but representative DE simulations. The strain field was then combined with a rheology for flowing granular material and linear momentum balance to yield estimates for the ploughing forces. We selected a simple constitutive description to minimize the number of fitting parameters.

Ploughing forces were computed for a range of plough velocities. We saw that inertial effects played a negligible role at low velocities, but dominated at high velocities. Results from ESPM compared well with studies of Coetzee & Els (2009) and Obermayr *et al.* (2011). Although our DE simulations that fed into ESPM were uncalibrated and employed circular grains, as opposed to the complex clumped grains utilized by Coetzee & Els (2009) in their calibrated DE simulations, forces predicted by ESPM showed a good match. Our own experiments were also in excellent agreement with ESPM results.

The present work may be augmented in several ways. The study was limited to two dimensions, but can be extended to three dimensions. Here, we utilized a simple constitutive model for the flowing grains as a first step. More comprehensive rheological models can lead to better results. Finally, only cohesionless grains are considered here. To address ploughing in cohesive granular media cohesion will have to be included in DE simulations that provide kinematic data to ESPM.

Acknowledgements

We thank Dr Ashish Bhateja (IIT Goa) for help with DE simulations and Shri Satya Prakash Mishra and Shri Amit Gaur for help with our experiments. S.M. and P.S. thank the Ministry for Human Resource and Development, Government of India for financial help through student scholarship. I.S. thanks Dr Kiran Akella (R&D Engineers, Pune) for bringing to our notice the problem addressed in this paper.

Appendix A. Effect of grid size

Figure 23 shows the variation in the components of strain rates when the size of the grid in figure 4 is modified. We observe that the change in the strain rates is small when the grid size is decreased from 0.5 to 0.25 non-dimensional units. Thus, we employ a grid size of 0.5 non-dimensional units to find the continuum velocity field $V(x, y, t)$ associated with the ploughed granular material.

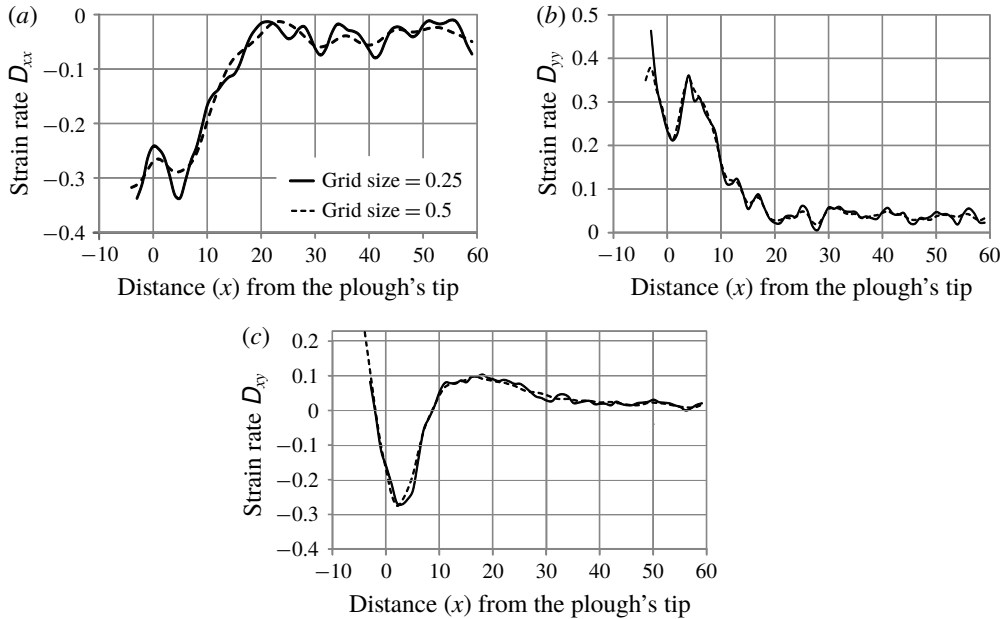


FIGURE 23. Components of the strain rate tensor at points along the line $y = 9$ with different grid sizes. The tip of the plough is at $x = 0$. (a) Normal strain rate D_{xx} . (b) Normal strain rate D_{yy} . (c) Shear strain rate D_{xy} . The plough's non-dimensional speed $v_c = 10$, the inter-grain friction $\mu = 0.3$ and grain diameter $d = 0.67$.

Appendix B. Granular flow down an inclined plane

Here we investigate the flow of grains down an inclined plane and compare the predictions of ESPM with direct DE simulations and theoretical estimates obtained from the $\mu(I)$ -rheology (MiDi 2004). The $\mu(I)$ -rheology assumes that shear stress depends only on the local shear rate and is expressed in terms of friction coefficient μ and volume fraction ϕ depending on a single dimensionless number – the inertial number I . Jop *et al.* (2006) utilized this rheology to put forward a three-dimensional, viscoplastic description of granular flow. Employing the $\mu(I)$ -rheology in the steady uniform regime for granular flow down an inclined plane, Pouliquen & Forterre (2009) found the normal stress P and shear stress τ to be, respectively,

$$P(z) = \rho_p \phi g \cos \theta (h - z) \quad \text{and} \quad \tau(z) = \rho_p \phi g \sin \theta (h - z), \quad (\text{B } 1)$$

where θ is the inclination angle of the plane, h is thickness of the flow in the z direction and ϕ is the volume fraction, which was shown to be an unknown constant through the flow's depth. The velocity profile $u(z)$ was found to be the Bagnold profile:

$$u(z) = I(\tan \theta) \frac{2}{3} \frac{\sqrt{\phi g \cos \theta}}{d} \{h^{3/2} - (h - z)^{3/2}\}, \quad (\text{B } 2)$$

which requires a knowledge of the inertial number I .

To apply ESPM, we perform two-dimensional DE simulations considering a system of polydispersed, steady granular flows with 2100 grains. The length l of the base and the thickness h of the flow are, respectively, $20d$ and $100d$, where d is the diameter

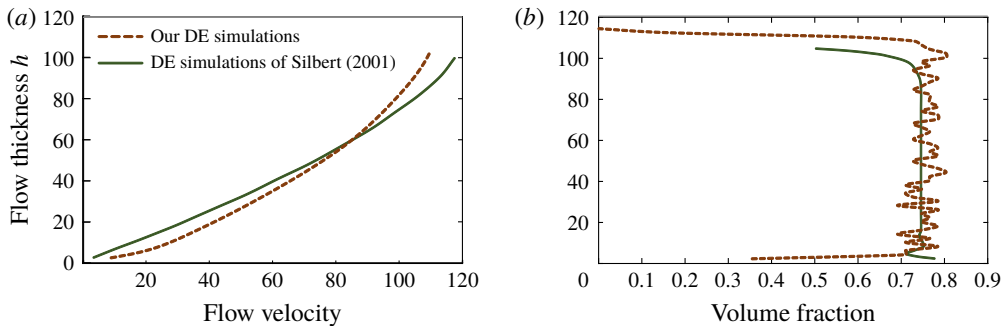


FIGURE 24. (Colour online) Comparison of (a) velocity and (b) volume fraction profiles obtained from our DE simulations and those of Silbert *et al.* (2001).

of the larger grain. The base is inclined at an angle $\theta = 22^\circ$, and this corresponds to flows that fall within the regime in which the constitutive law of § 5.1 is applicable. Our DE simulations will provide kinematic information to be utilized in subsequent ESPM calculations.

Our DE simulations parallel the L2 model of Silbert *et al.* (2001), with the following differences: (i) we use a smoother base, (ii) tangential springs are absent and (iii) the coefficient of restitution is lower (0.82 instead of 0.92). Figure 24(a) shows the velocity profiles obtained from our DE simulations and those of Silbert *et al.* (2001). We find a higher velocity near the base than that of Silbert *et al.* (2001) because we use a smoother base, while the greater grain inelasticity in our simulations is probably responsible for the reduction in velocity at the top of the flow. Nevertheless, our velocity profile agrees well with Silbert *et al.* (2001), and matches the Bagnold profile. We are unable to utilize the velocity profile (B 2) for comparison, because this requires knowledge of the inertial number for two-dimensional inclined plane flows, which is unavailable.

The volume fraction ϕ found from DE simulations is shown in figure 24(b), and again a close match is observed between our results and those of Silbert *et al.* (2001). Theoretically, Pouliquen & Forterre (2009) predict that the volume fraction is constant through the bulk, although the volume fraction itself was not predicted, and is found from experiments or simulations. This prediction matches simulations except near the top and bottom of the flow. The discussion so far confirms the correctness of the kinematics predicted by our DE simulations.

Now, we utilize ESPM to find the normal and shear stress, and compare with theoretical predictions (Pouliquen & Forterre 2009) and direct DE simulations (Silbert *et al.* 2001). Both we and Silbert *et al.* (2001) find the bulk volume fraction ϕ to be approximately equal to 0.76. This estimate of the volume fraction will be utilized in (B 1). Figure 25 compares the stresses obtained by employing ESPM (using the deformation field from our DE simulations) with those found from the direct DE simulations of Silbert *et al.* (2001), and from the $\mu(I)$ -rheology. We find a good quantitative agreement between the direct DE simulations of Silbert *et al.* (2001) and ESPM. The manner in which the base is modelled in DE simulations is perhaps the reason behind the observed mismatch, especially in the shear stress in figure 25(b). The $\mu(I)$ -rheology tends to under-predict both normal and shear stresses, but the match is still reasonable.

The above analysis demonstrates the ability of ESPM to recover theoretical and direct computational results in the context of a well-studied granular system.

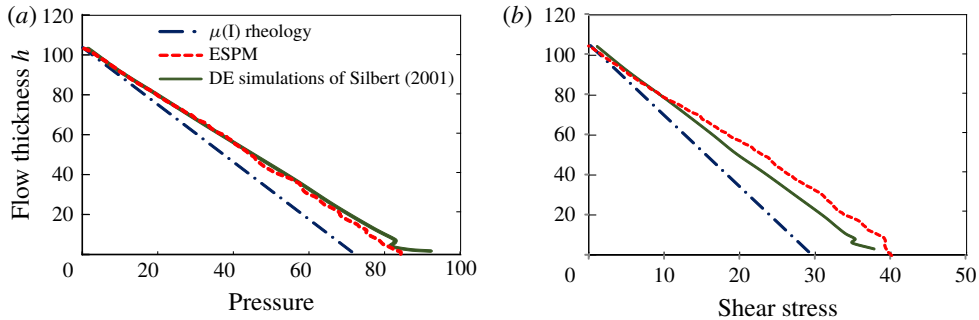


FIGURE 25. (Colour online) Comparison of stress fields. (a) Normal stress and (b) shear stress. For $\mu(I)$ -rheology, we used $\phi = 0.76$, obtained from simulations.

REFERENCES

- AGUILAR, J., ZHANG, T., QIAN, F., KINGSBURY, M., MCINROE, B., MAZOUCHOVA, N., LI, C., MALADEN, R., GONG, C., TRAVERS, M. *et al.* 2016 A review on locomotion robophysics: the study of movement at the intersection of robotics, soft matter and dynamical systems. *Rep. Prog. Phys.* **79** (11), 110001.
- ALEKSEEVSKII, V. P. 1966 Penetration of a rod into a target at high velocity. *Fizika Goreniya I Vzryva (translated Combustion, Explosion, and Shock Waves, pp. 63–66)* **2**, 99–106.
- ASAF, Z., RUBINSTEIN, D. & SHMULEVICH, I. 2007 Determination of discrete element model parameters required for soil tillage. *Soil Till. Res.* **92** (1), 227–242.
- ASKARI, H. & KAMRIN, K. 2016 Intrusion rheology in grains and other flowable materials. *Nat. Mater.* **15** (12), 1274–1279.
- BALIGH, M. M. 1985 Strain path method. *J. Geotech. Engng* **111** (9), 1108–1136.
- BARKER, T., SCHAEFFER, D. G., BOHORQUEZ, P. & GRAY, J. M. N. T. 2015 Well-posed and ill-posed behaviour of the mu-rheology for granular flow. *J. Fluid Mech.* **779**, 794–818.
- BHARADWAJ, R. L., WASSGREN, C. & ZENIT, R. 2006 The unsteady drag force on a cylinder immersed in a dilute granular flow. *Phys. Fluids* **18** (4), 043301.
- BHATEJA, A., SHARMA, I. & SINGH, J. K. 2016 Scaling of granular temperature in vibro-fluidized grains. *Phys. Fluids* **28** (4), 043301.
- BHATEJA, A., SHARMA, I. & SINGH, J. K. 2017 Segregation physics of a macroscale granular ratchet. *Phys. Rev. Fluids* **2** (5), 052301.
- BIRKHOFF, G., MACDOUGALL, D. P., PUGH, E. M. & TAYLOR, G. 1948 Explosives with lined cavities. *J. Appl. Phys.* **19**, 563–582.
- COETZEE, C. J. 2014 Discrete and continuum modelling of soil cutting. *Comput. Part. Mech.* **1** (4), 409–423.
- COETZEE, C. J. 2017 Calibration of the discrete element method. *Powder Technol.* **310**, 104–142.
- COETZEE, C. J. & ELS, D. N. J. 2009 Calibration of granular material parameters for DEM modelling and numerical verification by blade–granular material interaction. *J. Terramechanics* **46** (1), 15–26.
- CRANDALL, S. H., DAHL, N. C. & DILL, E. H. 1960 *An Introduction to the Mechanics of Solids*. McGraw-Hill.
- CUNDALL, P. A. & STRACK, O. D. L. 1979 A discrete numerical model for granular assemblies. *Géotechnique* **29** (1), 47–65.
- DING, Y., GRAVISH, N. & GOLDMAN, D. I. 2011 Drag induced lift in granular media. *Phys. Rev. Lett.* **106** (2), 028001.
- GOLDREIN, H. T., GRANTHAM, S. G., PROUD, W. G. & FIELD, J. E. 2002 The study of internal deformation fields in granular materials using 3D digital speckle x-ray flash photography. *AIP Conf. Proc.* **620**, 1105–1108.

- GOLDREIN, H. T., PALMER, S. J. P. & HUNTLEY, J. M. 1995 Automated fine grid technique for measurement of large-strain deformation maps. *Opt. Lasers Engng* **23** (5), 305–318.
- GRANTHAM, S. G., PROUD, W. G., GOLDREIN, H. T. & FIELD, J. E. 2006 Study of internal deformation fields in granular materials using 3D digital speckle x-ray flash photography. In *Laser Interferometry X: Techniques and Analysis*, vol. 4101, pp. 319–327. International Society for Optics and Photonics.
- GRAVISH, N., UMBANHOWAR, P. B. & GOLDMAN, D. I. 2010 Force and flow transition in plowed granular media. *Phys. Rev. Lett.* **105** (12), 128301.
- GRAVISH, N., UMBANHOWAR, P. B. & GOLDMAN, D. I. 2014 Force and flow at the onset of drag in plowed granular media. *Phys. Rev. E* **89** (4), 042202.
- GUO, H., GOLDSMITH, J., DELACRUZ, I., TAO, M., LUO, Y. & KOEHLER, S. A. 2012 Semi-infinite plates dragged through granular beds. *J. Stat. Mech. Theory Exp.* **2012** (07), P07013.
- HETTIARATCHI, D. R. P. & REECE, A. R. 1967 Symmetrical three-dimensional soil failure. *J. Terramechanics* **4** (3), 45–67.
- HETTIARATCHI, D. R. P., WITNEY, B. D. & REECE, A. R. 1966 The calculation of passive pressure in two-dimensional soil failure. *J. Agric. Engng Res.* **11** (2), 89–107.
- JOP, P., FORTERRE, Y. & POULIQUEN, O. 2006 A constitutive law for dense granular flows. *Nature* **441** (7094), 727–730.
- KATSURAGI, H. & DURIAN, D. J. 2013 Drag force scaling for penetration into granular media. *Phys. Rev. E* **87** (5), 052208.
- LI, C., UMBANHOWAR, P. B., KOMSUOGLU, H., KODITSCHKE, D. E. & GOLDMAN, D. I. 2009 Sensitive dependence of the motion of a legged robot on granular media. *Proc. Natl Acad. Sci. USA* **106** (9), 3029–3034.
- LI, C., ZHANG, T. & GOLDMAN, D. I. 2013 A terradynamics of legged locomotion on granular media. *Science* **339** (6126), 1408–1412.
- LIU, C. H., NAGEL, S. R., SCHECTER, D. A., COPPERSMITH, S. N., MAJUMDAR, S., NARAYAN, O. & WITTEN, T. A. 1995 Force fluctuations in bead packs. *Science* **269** (5223), 513–515.
- LORET DE MOLA LEMUS, D., KOHANBASH, D., MORELAND, S. & WETTERGREEN, D. 2014 Slope descent using plowing to minimize slip for planetary rovers. *J. Field Rob.* **31** (5), 803–819.
- MCKYES, E. 1985 *Soil Cutting and Tillage*, vol. 7. Elsevier.
- MCKYES, E. & ALI, O. S. 1977 The cutting of soil by narrow blades. *J. Terramechanics* **14** (2), 43–58.
- METCALFE, G., TENNAKON, S. G. K., KONDIC, L., SCHAEFFER, D. G. & BEHRINGER, R. P. 2002 Granular friction, coulomb failure, and the fluid-solid transition for horizontally shaken granular materials. *Phys. Rev. E* **65** (3), 031302.
- MIDI, G. D. R. 2004 On dense granular flows. *Eur. Phys. J. E* **14** (4), 341–365.
- MORELAND, S., SKONIECZNY, K., INOTSUME, H. & WETTERGREEN, D. 2012 Soil behavior of wheels with grousers for planetary rovers. In *2012 IEEE Aerospace Conference*, pp. 1–8. IEEE.
- MURTHY, T. G., GNANAMANICKAM, E. & CHANDRASEKAR, S. 2012 Deformation field in indentation of a granular ensemble. *Phys. Rev. E* **85** (6), 061306.
- MURTHY, T. G., SALDANA, C., YADAV, S. & DU, F. 2013 Experimental studies on the kinematics of cutting in granular materials. *AIP Conf. Proc.* **1542**, 919–922.
- NEDDERMAN, R. M. 1992 *Statics and Kinematics of Granular Materials*. Cambridge University Press.
- OBERMAYR, M., DRESSLER, K., VRETTOS, C. & EBERHARD, P. 2011 Prediction of draft forces in cohesionless soil with the discrete element method. *J. Terramechanics* **48** (5), 347–358.
- OLDROYD, J. G. 1947 A rational formulation of the equations of plastic flow for a Bingham solid. *Math. Proc. Camb. Phil. Soc.* **43**, 100–105.
- ONO, I., NAKASHIMA, H., SHIMIZU, H., MIYASAKA, J. & OHDOI, K. 2013 Investigation of elemental shape for 3D DEM modeling of interaction between soil and a narrow cutting tool. *J. Terramechanics* **50** (4), 265–276.
- PALMER, A. C. 1999 Speed effects in cutting and ploughing. *Gèotechnique* **49** (3), 285–294.

- PAWAR, H. 2013 Interaction laws in discrete element method. MTech thesis, Indian Institute of Technology, Kanpur, India.
- PERCIER, B., MANNEVILLE, S., MCELWAIN, J. N., MORRIS, S. W. & TABERLET, N. 2011 Lift and drag forces on an inclined plow moving over a granular surface. *Phys. Rev. E* **84** (5), 051302.
- PITMAN, E. B. & SCHAEFFER, D. G. 1987 Stability of time dependent compressible granular flow in two dimensions. *Commun. Pure Appl. Maths* **40** (4), 421–447.
- POULIQUEN, O. & FORTERRE, Y. 2009 A non-local rheology for dense granular flows. *Proc. R. Soc. Lond. A* **367** (1909), 5091–5107.
- PRAGER, W. 1961 *Introduction to Mechanics of Continua*. Ginn and Co.
- QIONG, G., PITT, R. E. & RUINA, A. 1986 A model to predict soil forces on the plough mouldboard. *J. Agric. Engng Res.* **35** (3), 141–155.
- R CORE TEAM 2013 *R: A Language and Environment for Statistical Computing*. R Foundation for Statistical Computing.
- RUBIN, M. B. 2012 Analytical formulas for penetration of a long rigid projectile including the effect of cavitation. *Intl J. Impact Engng* **40**, 1–9.
- SAURET, A., BALMFORTH, N. J., CAULFIELD, C. P. & MCELWAIN, J. N. 2014 Bulldozing of granular material. *J. Fluid Mech.* **748**, 143–174.
- SCHAEFFER, D. G. 1987 Instability in the evolution equations describing incompressible granular flow. *J. Differ. Equ.* **66** (1), 19–50.
- SCHAEFFER, D. G. 1990 Instability and ill-posedness in the deformation of granular materials. *Intl J. Num. Anal. Meth. Geomech.* **14** (4), 253–278.
- SCHAEFFER, D. G. & PITMAN, E. B. 1988 Ill-posedness in three-dimensional plastic flow. *Commun. Pure Appl. Maths* **41** (7), 879–890.
- SEGUIN, A., BERTHO, Y., GONDRET, P. & CRASSOUS, J. 2011 Dense granular flow around a penetrating object: experiment and hydrodynamic model. *Phys. Rev. Lett.* **107** (4), 048001.
- SEVENHUIJSEN, P. J., SIRKIS, J. S. & BREMAND, F. 1993 Current trends in obtaining deformation data from grids. *Expl Techn.* **17** (3), 22–26.
- SHARMA, I. 2017 *Shapes and Dynamics of Granular Minor Planets: The Dynamics of Deformable Bodies Applied to Granular Objects in the Solar System*. Springer International Publishing.
- SHARMA, I. 2019 High-speed impacts of slender bodies into non-smooth, complex fluids. *J. Fluid Mech.* **861**, R1.
- SHMULEVICH, I., ASAF, Z. & RUBINSTEIN, D. 2007 Interaction between soil and a wide cutting blade using the discrete element method. *Soil Till. Res.* **97** (1), 37–50.
- SILBERT, L. E., ERTAŞ, D., GREST, G. S., HALSEY, T. C., LEVINE, D. & PLIMPTON, S. J. 2001 Granular flow down an inclined plane: Bagnold scaling and rheology. *Phys. Rev. E* **64** (5), 051302.
- SLONAKER, J., MOTLEY, D. C., ZHANG, Q., TOWNSEND, S., SENATORE, C., IAGNEMMA, K. & KAMRIN, K. 2017 General scaling relations for locomotion in granular media. *Phys. Rev. E* **95** (5), 052901.
- SOKOLOVSKI, V. V. 1960 *Statics of Solid Media*. Butterworths Scientific Publications.
- TANAKA, H., MOMOZU, M., OIDA, A. & YAMAZAKI, M. 2000 Simulation of soil deformation and resistance at bar penetration by the distinct element method. *J. Terramechanics* **37** (1), 41–56.
- TATE, A. 1967 A theory for the deceleration of long rods after impact. *J. Mech. Phys. Solids* **15**, 387–399.
- TATE, A. 1969 Further results in the theory of long rod penetration. *J. Mech. Phys. Solids* **17**, 141–150.
- TATE, A. 1978 A simple hydrodynamic model for the strain field produced in a target by the penetration of a high speed long rod projectile. *Intl J. Engng Sci.* **16**, 845–858.
- TATE, A. 1986a Long rod penetration models. Part I. A flow field model for high speed long rod penetration. *Intl J. Mech. Sci.* **28**, 535–548.
- TATE, A. 1986b Long rod penetration models. Part II. Extensions to the hydrodynamic theory of penetration. *Intl J. Mech. Sci.* **28**, 599–612.

- THOMAS, B. J. & SCHAEFFER, D. G. 1988 Nonlinear behavior of model equations which are linearly ill-posed. *Commun. Partial Diff. Eq.* **13** (4), 423–467.
- TRIPATHI, A. & KHAKHAR, D. V. 2010 Steady flow of smooth, inelastic particles on a bumpy inclined plane: hard and soft particle simulations. *Phys. Rev. E* **81** (4), 041307.
- TSUJI, T., NAKAGAWA, Y., MATSUMOTO, N., KADONO, Y., TAKAYAMA, T. & TANAKA, T. 2012 3-D DEM simulation of cohesive soil-pushing behavior by bulldozer blade. *J. Terramechanics* **49** (1), 37–47.
- WETTERGREEN, D., MORELAND, S., SKONIECZNY, K., JONAK, D., KOHANBASH, D. & TEZA, J. 2010 Design and field experimentation of a prototype lunar prospector. *Intl J. Rob. Res.* **29** (12), 1550–1564.
- WIEGHARDT, K. 1975 Experiments in granular flow. *Annu. Rev. Fluid Mech.* **7** (1), 89–114.
- YADAV, S., SALDANA, C. & MURTHY, T. G. 2015 Deformation field evolution in indentation of a porous brittle solid. *Intl J. Solids Struct.* **66**, 35–45.
- YARIN, A. L., RUBIN, M. B. & ROISMAN, I. V. 1995 Penetration of a rigid projectile into an elastic-plastic target of finite thickness. *Intl J. Impact Engng* **16**, 801–831.